aerospace

MDPI

Article

An Analysis of a Complete Aircraft Electrical Power System Simulation Based on a Constant Speed Constant Frequency Configuration

Octavian Grigore-Müler

Faculty of Aerospace Engineering, National University of Science and Technology POLITEHNICA Bucharest, 060042 Bucharest, Romania; octavian.grigore@upb.ro; Tel.: +40-742040309

Abstract: Recent developments in aircraft electrical technology, such as the design and production of more electric aircraft (MEA) and major steps in the development of all-electric aircraft (AEA), have had a significant impact on aircraft's electrical power systems (EPSs). However, the EPSs of the latest aircraft produced by the main players in the market, Airbus with the Neo series and Boeing with the NG and MAX series are still completely traditional and based on the constant speed constant frequency (CSCF) configuration. For alternating current ones, the EPS is composed of the following: prime movers, namely the aircraft turbofan engine (TE); the electrical power source, i.e., the integrated drive generator (IDG); the command and control system, the generator control unit (GCU); the transmission and the system distribution system; the protection system, i.e., the CBs (circuit breakers); and the electrical loads. This paper presents the analysis of this system using the Simscape package from Simulink v 8.7, a MATLAB v 9.0 program, which is actually the development of some systems designed in two previous personal papers. For the first time in the literature, a complete MATLAB modelled EPS system was presented, i.e., the aircraft turbofan engine model, driving the constant speed drive system (CSD) (model presented in the first reference as a standalone type and with different parameters), linked to the synchronous generator (SG) (model presented in second reference for lower power and rotational speed) in the so-called integrated drive generator (IDG) and electrical loads.

Keywords: AEA; AFR; AVR; CSD; EPS; IDG; MEA; PID; turbofan; VSCF; VSVF

Citation: Grigore-Müler, O. An Analysis of a Complete Aircraft Electrical Power System Simulation Based on a Constant Speed Constant Frequency Configuration. *Aerospace* **2024**, *11*, 860. https://doi.org/10.3390/aerospace11100860

Academic Editor: Mona Ghassemi

Received: 18 September 2024
Revised: 8 October 2024
Accepted: 10 October 2024
Published: 18 October 2024

1. Introduction

From a historical point of view, electrical energy was first used onboard airplanes with the Wright brothers' first flight on 17 December 1903, and this was only to power the engine's ignition system [1,2], which was actually produced by a device called a magneto [3,4] considered, in fact, the first onboard electrical power supply. From this date, when the Wright brothers completed the first motorized, manned, heavier-than-air flight, it marked the beginning of a new era, the Era of Powered and Controlled Flight and also the Era of the Airplane's Electrical System. The next step was the beginning of commercial air transport, on 1 January 1914, when the first scheduled flight of a commercial airline, a Benoist flying boat, took off from St. Petersburg to Tampa in Florida, United States of America [5]. The plane was equipped with "primitive" flight instruments, including an inclinometer, a compass, an aneroid barometer, and a tachometer, which was the only one electrically operated [6,7] and powered by a battery. Just two months later, on 11 February 1914, the Sikorsky Ilya Muromets prototype (factory airframe 128), a four-engine airplane, took off from Moscow for its first demonstration flight with 16 passengers aboard, marking a record for the number of passengers carried. At this time in the history of aviation, the electrical energy needed for passengers was obtained for the first time from a DC electrical wind-driven generator rated at 200 W [8–10].

All onboard systems must first and foremost be reliable, as the completion of the flight mission depends upon them. Obviously, they have to be light because a reduction in weight actually means more payload or more fuel. They should also be relatively easy to maintain. The cost should not be excessive, although it takes into account requirements such as reliability and weight. With these requirements in mind, the next step was to drive the generator from the aircraft's engine. This was achieved on 4 July 1914 when a 150 W generator at 10 V was directly driven by the Liberty engine [11]. Thus, the introduction of the generator on board the aircraft could be considered the beginning of a new era, the Era of the Airplane's Electrical Power System.

At the beginning of this "Era", due to the lack of manufacturers of aviation electrical equipment, they were using parts from automobiles, hence the initial supply voltage of 10–15 V. The beginning of commercial air transport made flying more popular (the number of passengers and the amount of baggage had increased due to the shortening of travel times, compared to other modes of transport, and improved flight conditions), so the demand for electricity onboard increased. Thus, in 1933, the Boeing Airplane Co. (Arlington, VA, USA) manufactured the Boeing 247, considered by electrical aviation specialists to be the first modern passenger aircraft, in reference to the electrical power system. It had two DC generators rated at 750 W/15 V per unit [12]. Since an increase in power at a constant voltage requires a proportional increase in current, thicker wire cables are needed to carry it, meaning a greater weight of the onboard electrical network. An increase in the voltage of the generators takes into account that when the voltage is doubled, the weight of the wiring decreases four times. Thus, in 1934, 28–30 DC generators were chosen as the standard to power the DC EPS.

Towards the end of WWII, aircraft electrical engineers realized that the 28 low-voltage DC systems were no longer an option due to losses in weight, volume, and power in the electrical distribution network. Studies and research carried out in the early 1940s found that an AC EPS at a frequency of 400 Hz would be optimal, precisely because of the reduced weights of motors and generators without a significant increase in wire weight [13].

Thus, as the source of a power supply, the pole-wound synchronous generator (SG) was chosen as the standard generator for the aircraft's EPS precisely because of its inherent advantages in weight, size, performance (the highest electrical power per kilogram per rpm), and efficiency (due to its lowest reactance, the transient load performance is the best). Since the generator is of the synchronous type, the frequency of the alternating current's voltage is proportional to the rotational speed of the generator, so a method of converting the variable speed of the aircraft engine to a constant one is required when dealing with fixed frequency systems. So, the first CSCF configuration was born. Later, electrical aviation engineers designed and developed other EPS configurations, including VSCF (variable speed constant frequency) and, more recently, VSVF (variable speed variable frequency), as shown in Figure 1. In the VSCF configuration, the electrical power that supplies the loads is generated by some static power converters, which are supplied with variable speed/frequency power by the direct engine-driven generator through a gearbox. Depending on the type of converters, this configuration can have three options:

- A cycloconverter (Cyclo) VSCF that uses an AC-to-AC converter;
- A DC link VSCF that uses a DC-to-AC converter;
- A 270 VDC VSCF that uses an AC-to-DC converter.

Because of the advantages of the CSCF configuration, including its increased reliability (millions of hours of operation on various aircraft with an MTBF of 30,000 h [12,14]), light weight, and simple maintenance, the CSCF 115/200 V AC at a 400 Hz frequency was chosen to be the standard for the aircraft electrical power systems and has remained the same to the present day (about 90.69% of commercial airliners in service in 2024 were equipped with it, as shown in Figure 2) [15].

In the AC CSCF configuration shown in Figure 3, the primary electrical power is generated by a three-stage brushless SG (BSG). It is driven at a constant speed by a CSD, led

in turn by the aircraft's turbofan engine through a gearbox, at a variable speed, depending on the propulsion power of the engine in different phases of the flight.

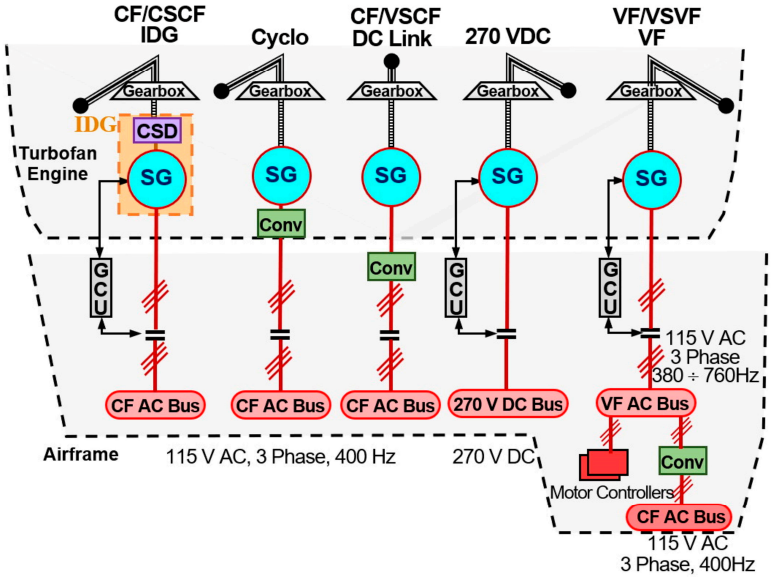

Figure 1. The typical EPS configurations [2].

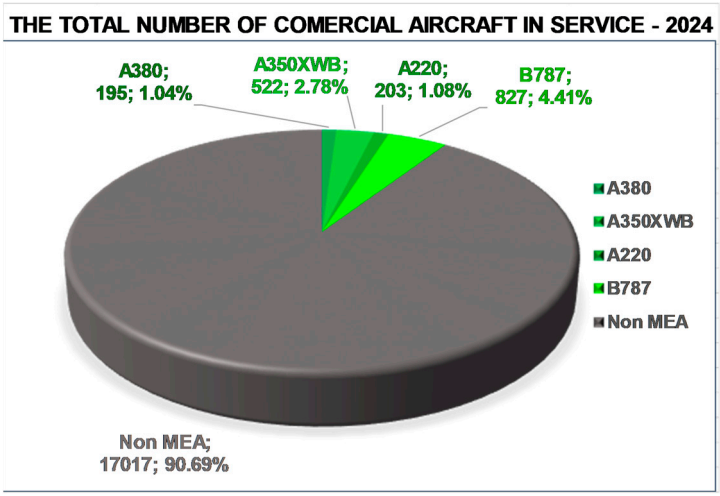

Figure 2. The total number of commercial airplane MEA and non-MEA in service in 2024 (data from [15]).

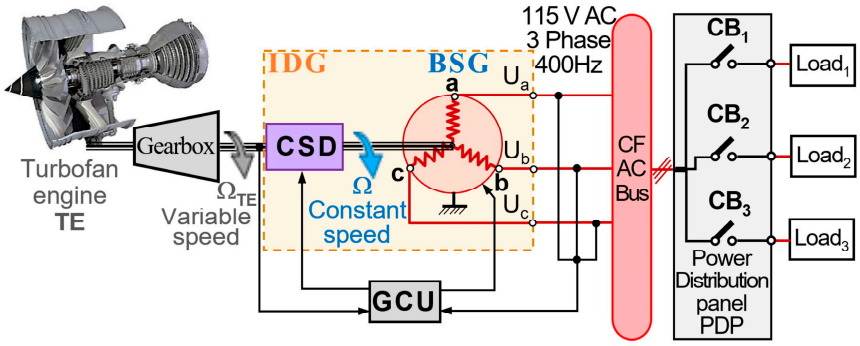

Figure 3. The EPS architecture of a CSCF AC configuration [2].

From a historical point of view, the first major AC EPS was probably installed onboard the Brabazon Mark I airplane, built by the Bristol Airplane Company (presently BAE Systems Plc. Company (London, England)), with first flight on 6 September 1949.

2. Aircraft Turbofan Engine Mathematical Model

Generally, there are only two types of prime movers for airplanes: the heat engine and, more recently, the electrical engine, adopted by the aviation industry to meet the standards set up by ICAO-Corsia and ACARE. Today, heat engines such as the piston engines and more recently electric engines (i.e., Alice from Eviation Aircraft (Arlington, WA, USA)) that drive propellers are used in small airplanes, whereas the heat engines such the turbines power most other aircraft, more precisely all transport airplanes.

All turbine engines have as common features an air compressor, a combustion chamber and a turbine assembly. According to the arrangement of these components, the following types of turbine engines are used in aviation:

- The jet engines are those with a single shaft that connects the turbine to the compressor;
- The low-bypass ratio engines for which the compressor is divided into several separate parts, each of them driven by individual turbine/shaft assemblies;
- The afterburning jet engines that increase the output jet by injecting and burning additional fuel between the turbine and the nozzle to increase performance;
- The turbofan engines, a development of the bypass jet engine with a substantial increase in compressor's first stage diameter to become a ducted fan;
- The turboprop/turboshaft engines for which the turbine stage is normally divided into two parts, the high-pressure turbine (HPT) and the low-pressure turbine (LPT), respectively. Each of them drive individual concentric shafts; LPT drives the power output shaft that has a physical/remote gearbox to connect the propeller;
- The ramjet engines, which are made of an inlet, a combustion zone and a nozzle, and have no moving parts (compressor and turbine).

From a historical point of view, jet propulsion started in very early times when, around 250 BC, Hero of Alexandria invented the "aeolipile", which was considered the first documented reaction-type turbine. This was followed by other discoveries in the field, including, amongst them, the following: the first rocket launch by Chinese inventor Wan Hu (1232), the sketch of "chimney jack" machine by the well-known Italian inventor and scientist Leonardo da Vinci, the first impulse turbine developed by the Italian engineer Giovanni Branca (1629) and Newton's steam wagon made by the Dutchman Jacob Gravesand (1687) [16].

In the field of gas turbines, the first patent for an engine with both a classical architecture (consisting of a compressor, a turbine and a combustion chamber) and a thermodynamic cycle of a modern gas turbine was awarded in 1791 to the Englishman John Barber [16]. In 1903, the American Sanford Alexander Moss received his PhD degree from Cornell University with a work on gas turbines. Later, when he joined General Electric Co. (GE), by 1907, he designed and built a real one, but the performance was poor. Around the same time in France, Loren wrote an article about the possibility of jet propulsion that marked the earliest known mention about it. Between 1900 and 1906, he founded a company in France, known as Sociétè Anonyme des Turbomoteurs (Saint-Denis, Paris, France). This was taken over by an inventor, Lemale, and an attorney, (Rene) Armengaud, who, after reorganizing it, designed and built a gas turbine with a centrifugal-type compressor. The compressor was designed and built by Brown-Boveri Company (BBC) (Baden bei Zürich, Switzerland), and though the turbine worked, its efficiency was only 3%. This was in fact about 2% below the efficiency of the steam locomotive; thus, it had no future utility, and it was abandoned [17]. Between 1905 and 1940, the BBC of Zurich designed and built several pioneering gas turbines.

In aeronautics, the idea of jet engine propulsion started in 1910 when Henri Marie Coanda, a Romanian engineer and inventor, "a venerable pioneer in aviation, thoroughly unknown outside of Europe but a man who had done a great deal in aircraft progress" [18],

designed and built "Coanda 1910", a jet engine airplane. This was exhibited at the Parisian Aeronautical Exhibition in 1910, but while it was lifted off the ground, then turned again, unfortunately, it broke down at landing. Coanda decided not to rebuild it and he did not continue any further work [18–20].

Finally, as the aviation historians recognize, the real aircraft gas turbine was developed by two geniuses, Frank Whittle (in Great Britain) and Hans von Ohain (in Germany), who independently invented and manufactured it [21]. During WWII, the British shared their gas turbine technology with the United States, and this collaboration led to the foundation of the U.S. aircraft gas turbine industry. What is lesser known is that three indigenous U.S. gas turbine concepts developed by Vladimir Pavlecka and Frederick Dallenbach, for Northrop Aircraft Co. (Hawthorne, CA, USA), and Nathan Price for Lockeed Aircraft Corp. (Burbank, CA, USA) [22], were contemporaries with Whittle and von Ohain's invention. Based on von Ohain's design on 17 August 1939, the first successful flight of the He178 jet-powered aircraft was made. On the other site, on 15 May 1941, the Gloster E28/39 powered with the Whittle engine design took off [16].

All the forms of propulsion described above develop thrust, the primary goal of prime movers; this is achieved by pushing air backwards (or hot gases), while a small part of the mechanical power is used to generate electrical and hydraulic power via an accessory gearbox. In a simplified case, by neglecting the turbine's thermodynamics, the resultant force is given by Newton's second law of motion (which states that the sum of forces that act upon a body is proportional to the rate of change of momentum ($p = mV$)), where the constant of proportionality is 1/k:

$$\sum F = \frac{1}{\mathrm{k}} \frac{d(mV)}{dt} = \frac{1}{\mathrm{k}} \frac{dp}{dt}. \tag{1}$$

The constant k is practically a dimensional constant, depending on the measurement system; thus, k = 1 for terms in SI and k = 32.174 for English units, respectively.

To determine an expression for engine thrust, a control volume (cv) that surrounds the engine is chosen, and the momentum principles of the fluid flow crossing the boundaries of the control volume are applied. For simplification, the cv was chosen to have the same exit surface with the engine's nozzle, and the front surface the same with the inlet, so that, in this way, its inlet is far from the engine's one and is not disturbed by the nacelle's lip. Thus, the pressure at the cv inlet is uniform and equal to the atmospheric pressure p_a, as shown in Figure 4. The air stream tube enters in the engine with the velocity u_a (which is actually the airplane's airspeed), uniformly across the area $\mathrm{A_0}$ + $\mathrm{A_1}$ from section ❶, through first area the air enters into the core, and through the second into the fan. Because the volume of air that enters the fan can be divided so that a portion exits through the fan's exhaust and another is mixed into the core and exits through the nozzle, two exit areas must be considered. Therefore, in section ❷, at the fan's exit, the velocity and pressure are u_s and p_s, respectively, and in section ❸, at the core engine's exhaust, the velocity and pressure are u_e and p_e, respectively. The areas of sections ❷ and ❸ are A_s and A_e, respectively. In section ❷, the velocity and pressure are still u_a and p_a, respectively, except for the fan's exit area A_s. The fuel is injected at a flow rate of $\dot{m}_f$. The x and y directions chosen are parallel and normal to the centerline of the airplane's engine.

According to the linear momentum, the equation in rectangular coordinates is:

$$\sum F_\mathrm{s} + \sum F_\mathrm{b} = \frac{\partial}{\partial t} \iiint V \rho d\nu + \oiint V \rho V dA. \tag{2}$$

In Equation (2), F_s is the surface forces given by the pressures acting on the cv, T is the force acting on the engine's pylon (actually is the traction force), and F_b is the body forces.

Assuming a steady flow (thus, the partial derivative terms will disappear), Equation (2) in the x-direction will become:

$$\begin{aligned} T + p_a A_1 + p_a A_0 - p_a A_2 - p_s A_s - p_e A_e - p_a A_3 + F_{bx} = \\ -u_a \rho_a A_0 u_a + u_e \rho_e A_e u_e + u_s \rho_s A_s u_s - u_a \rho_a A_1 u_a + \\ u_a \rho_a A_2 u_e + \dot{m}_r u_a - \dot{m}_f u_{fx}. \end{aligned} \tag{3}$$

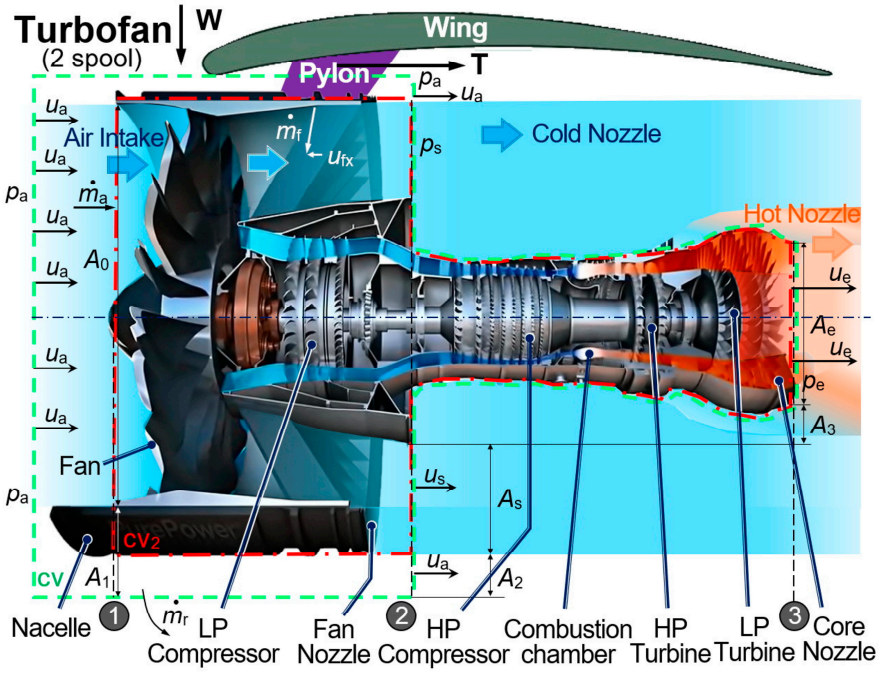

Figure 4. Schematic representation of a gas turbine engine with a control volume around it to determine the thrust.

By examining cv in Figure 4, it can be written that:

$$A_1 + A_0 = A_2 + A_3 + A_s + A_e. \tag{4}$$

If $\dot{m}_a$ is the total airflow entering the engine, $\dot{m}_s$ is the fan's (or secondary) exhaust airflow, and $\dot{m}_e$ the primary exhaust air flow, then:

$$\dot{m}_a = \rho_a A_0 u_a \; \dot{m}_s = \rho_s A_s u_s \; \dot{m}_e = \rho_e A_e u_e. \tag{5}$$

Taking into account the fact that in the x direction the force of the body is zero, Equation (4) becomes [21]:

$$T = A_e(p_e - p_a) + A_s(p_s - p_a) - \dot{m}_a u_a + \dot{m}_s u_s + \dot{m}_r u_a - u_a^2 \rho_a (A_1 - A_2) - \dot{m}_f u_{fx}. \tag{6}$$

Considering the continuity equation applied to a control volume (cv_2) that not only surrounds the engine, but also to cv,

$$\dot{m}_e + \dot{m}_s = \dot{m}_a + \dot{m}_f \tag{7}$$

$$\dot{m}_e + \dot{m}_s + \rho_a u_a A_2 + \dot{m}_r = \dot{m}_a + \dot{m}_f + \rho_a u_a A_1 \;\Rightarrow \tag{8}$$

$$\dot{m}_r = \rho_a u_a (A_1 - A_2), \tag{9}$$

as well as the fact that the x-direction component of the fuel velocity is small, it can be neglected; then, from Equations (6) and (9), the general equation of the thrust of a turbofan engine with an exhausted fan is given by:

$$T = A_e(p_e - p_a) + A_s(p_s - p_a) - \dot{m}_e(u_e - u_a) + \dot{m}_s(u_s - u_a) + \dot{m}_f u_a. \quad (10)$$

Considering that the fuel's flow is very small compared to the total airflow ($\dot{m}_f \ll \dot{m}_a$), by neglecting it in Equation (10), the reduced equation of the turbofan's force will be obtained:

$$T = A_e(p_e - p_a) + A_s(p_s - p_a) - \dot{m}_e(u_e - u_a) + \dot{m}_s(u_s - u_a). \quad (11)$$

From both equations, it can be seen that the thrust is composed of four terms: the first one is the force generated by the pressure differences at the primary exhaust, the second is given by the fan exhaust's pressures, and the third and fourth by the mass flows in the primary exhaust and the fan exhaust, respectively.

3. Mathematical Model of Integrated Drive Generator

As seen in Figure 1, the CSD system is the heart of a CSCF configuration, a system that is currently an integral part of an IDG (see Figure 5).

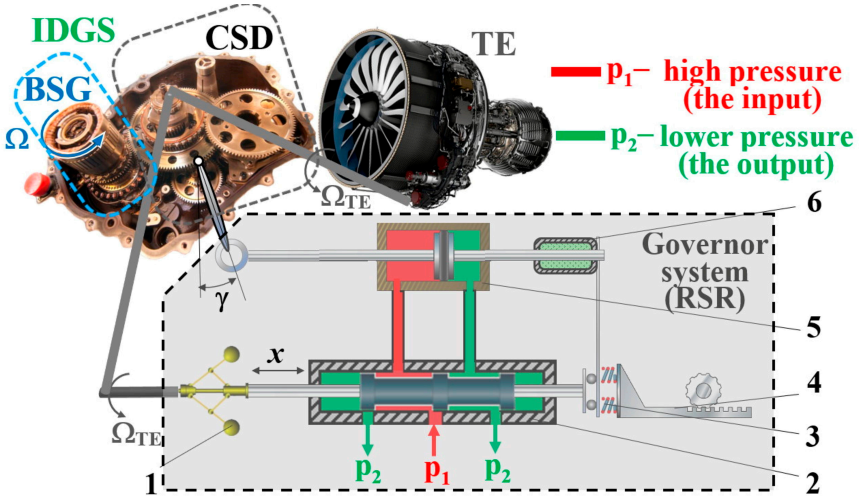

Figure 5. The block diagram of IDGS and governor system [2]: 1—centrifugal transducer; 2—measuring device (distributor)—two-way spool valve; 3—calibrating device (spring); 4—device for tuning centrifugal element; 5—hydraulic servomotor; 6—feedback mechanism.

As previously mentioned, following research studies carried out in the 1940s, it was concluded that the most efficient and reliable EPS for future aircraft is using alternating current at 400 Hz constant frequency powered by synchronous generators.

As these types of generators can provide only electrical power at a constant drive speed corresponding to the rated frequency, meaning that the engine's speed ranging from the idle on the ground to the maximum thrust at take-off is, therefore, critical. In order to optimize the design so that it can deliver the same power both at idle and at take-off, a generator drive system, a kind of constant speed converter (CSD), had to be developed.

3.1. Constant Speed Drive (CSD)

Since this device is what made the difference in the existence of a reliable AC EPS (found on board of 90.69% of all aircraft in service, see Figure 2), it is useful to recall its classification and evolution.

Depending on the type of transformed energy used to accommodate the variable speed to a fixed speed, CSDs can be either mechanical or hydraulic. Taking into account the percentage of energy transformed, they could be of direct drive, when the mechanical energy from an aircraft engine (AE) is completely transformed into another form of energy (usually hydraulic), and of differential drive, when the energy from an AE is partially transformed into another form, with most of the mechanical energy transferred directly by a planetary gear (differential) to the SG; in this way, the differential ones achieve higher efficiency than those with direct transmission. The last type of CSD, in which part of the mechanical energy is transformed into hydraulic energy, is also called axial gear differential (AGD). Finally, depending on the construction type, the CSDs can be either a stand-alone device (CSD) or integrated with the generator, called IDG. The AGD and IDG side by side (IDGS) belong to the last category.

In terms of evolution, the idea of a machine that can automatically change the input rotational speed was first mentioned in Gölz's 1935 US2114076 patent. In the early 1940s, the mechanical engineer Gunnar Wahlmark from Sundstrand Machine Tool Co (Rockford, IL, USA), with experience in machine tools and oil pumps, designed and patented (US2360025) a hydraulic automatic transmission for automobiles. Later, at the request of the air force, Sundstrand adapted this equipment to convert the variable rotational speed of the aircraft's engine into constant speed. In 1946, this device, weighing 2.48 kg/kW with a reliability of 3500 h MTBF, was installed onboard the Boeing B-36 bomber [12,23,24]. In early 1961, General Electric Company Ltd. (GEC) (Evendale, OH, USA) developed a ball pump CSD that was tested on the 2 × 20 kVA electrical system of the McDonnel YF4H Phantom aircraft. The GEC had a compact radial-piston hydrostatic transmission, including free spherical pistons, connecting rods and associated bearings. The concept demonstrated a reliability of 0.9997 per hour in over half a million hours of operation in aircraft applications [25,26]. Another concept was the fully mechanical drive type, developed in 1969 by English Electric Co Ltd. (London, England) [27]. An updated version of the unit was made 10 years later by Lucas Aerospace Co. (Birmingham, England) (used in the US Marine Harrier aircraft, AV-8A, with an 11/20 kVA electrical system) [28] and, recently, in 2007, by the Japanese at Kawasaki Heavy Industries Company (Minato, Tokyo, Japan), which built a device, called Traction Drive IDG (T-IDG) [29], that drives the generators of the military aircraft of the Japan Self-Defense Forces, the P-1 (22 units in service [30]) and XC-2 (10 units [31]). From all these, Sundstrand's concept was chosen as the basis for the development of the CSCF configuration, which, after further continuous developments, led to the current configuration of the AC EPS system presently used for most aircraft. In the early 1960s, the AGD, the differential hydraulic system, was developed with a weight of about 1.56 kg/kW and reliability of 12,000 h MTBF [32]. Also, in 1964, the first IDG was invented, by introducing the CSD and BSG systems in the same housing, which led to a weight reduction to 0.68 kg/kW and a reliability of 20,000 h MTBF [24]. Later, to improve the performance, the arrangement of devices was changed, by mounting them side by side. As a result, in early 1977, Lucas [33], and in 1978, Sundstrand [34], respectively, developed the integrated drive generator system (IDGS) weighing 0.44 kg/kW with a reliability of 30,000 h MTBF [14].

To determine the mathematical model of the differential hydro-mechanical CSD component of an IDGS, the sketch in Figure 6 will be used as well as Sundstrand's patent [35].

The device contains two hydraulic machines, the first one being the variable hydraulic unit (VHU) with a variable hydraulic displacement controlled by a variable angle disc 8, and the other, the fixed hydraulic unit (FHU), having a fixed angle disc 4 with a fixed displacement and a mechanical differential planetary gear 6 that performs the function of summing the speed of the input and output gears, respectively.

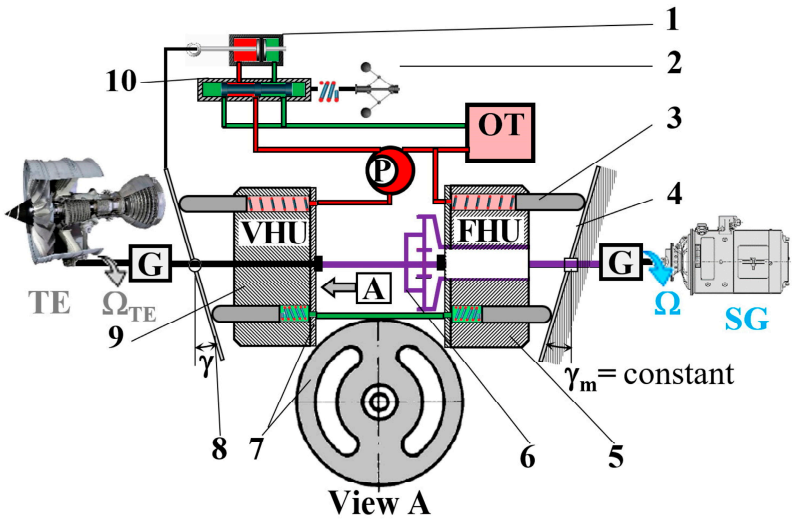

Figure 6. Sketch of a differential hydraulic CSD [1]; P—pump; G—gear box; OT—oil tank; 1—hydraulic actuator; 2—centrifugal transducer; 3—piston; 4—fixed disc of FHU; 5—FHU rotor; 6—the mechanical differential planetary gear; 7—the suction washer of the suction and discharge channels (distribution element); 8—variable angle wobbler of VHU (swash plate); 9—VHU rotor; 10—the distributor.

Because the angle of disc 8 varies continuously in both directions (from a positive to a negative angle), the VHU will move continuously from zero to maximum with displacement in both directions. The FHU is driven by the oil delivered by the VHU acting as a hydraulic pump. Therefore, it will operate at any speed, from zero to the maximum rated speed in both directions. The working pressure between the two hydraulic units is proportional to the torque transmitted to the generator.

Assuming that the input speed is lower than the rated speed, then the disc angle of the VHU is adjusted so that it feeds the flow to the FHU, so that its speed is added to the differential input speed. In this case, the VHU operates as a hydraulic pump (HP), and the FHU is a hydraulic motor (HM). The fixed-toothed ring, engaged with the fixed hydraulic unit, will rotate in the opposite direction to the bearing shaft, thus adding to the output speed. This condition is known as overdrive.

If the input speed is higher than the nominal one, a condition known as underdrive, the principle of operation is reversed from the overdrive condition.

At the nominal input speed, the torque is transmitted directly through the differential unit 4, and the FHU does not rotate. However, to prevent accidental leaks from the systems, the variable hydraulic drive disc will be slightly offset from the zero angle so that some fluid will be pumped to the FHU system.

To determine the mechanical characteristic of the CSD, a sketch of one of the hydraulic units (as shown in Figure 7) will be used. This is composed of a discrete number of pistons N that move in a sinusoidal motion to get the fluid moving. Due to this special design, the fluid flow output of an axial-piston pump is not a smooth straight line. Still, it tends to maintain some of the sinusoidal characteristics of the fluid displacement elements themselves. These are usually called the flow ripple of the pump and are suspected for generating additional vibration and noise [36]. It is assumed that the pump operation begins when one piston is at the zero-reference line, called the ”top dead center” (TDC). In this position, the fluid of the piston chamber will begin to be compressed [37].

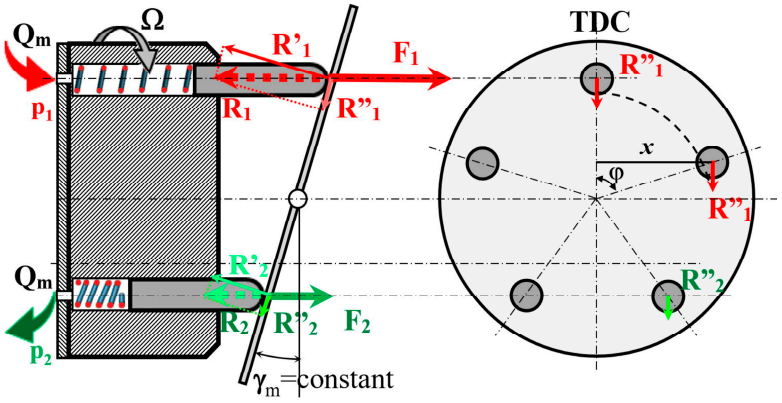

Figure 7. Sketch of the forces acting on CSD fixed disc [1].

The VHU hydraulic fluid flow expression is [38]:

$$Q_p = (1/120\pi)\Omega_p hSN, \tag{12}$$

where: Ω_p is the angular velocity, h—piston stroke, N—piston number, S—piston cylinder area.

If R is the distance from the center of the piston shaft to the rotor shaft, then h is:

$$h = 2Rtg\ \gamma. \tag{13}$$

Introducing Equation (13) in Equation (12), we obtain the following:

$$Q_p = (SNRtg\ \gamma/60\pi)\Omega_p = C_p\Omega_p tg\ \gamma, \tag{14}$$

where: $C_p = (SNR)/60\pi$ is a constant.

From Equation (14), it can be seen that to obtain a constant flow at a variable speed, the inclination angle γ of the disc must be changed. If the VHU's flow rate is constant, then the FHU's flow rate will be constant. As the pump and the hydraulic motor are reversible machines, then the angular velocity of the FHU is:

$$\begin{gathered} Q_m = (SNRtg\ \gamma_m/60\pi)\Omega_m = 1/C_m\Omega_m \implies \\ \Omega_m = C_m Q_m. \end{gathered} \tag{15}$$

Due to losses in the hydraulic circuit of the CSD (possible leakages), the flow rate of FHU, Q_m, is not equal to that of VHU, Q_p. Assuming that all leakage flows are laminar and have a linear relationship between pressure drop and flow, then the flow rate of the FHU becomes:

$$Q_m = Q_p - K_p \cdot p_1 = Q_p\left(1 - \frac{K_p \cdot p_1}{Q_p}\right), \tag{16}$$

where K_p is the coefficient of losses in the hydraulic circuit of the CSD and p_1 is high operating pressure of the hydraulic fluid.

The value $\frac{K_p \cdot p_1}{Q_p}$ in Equation (16) is practically the loss from the circuit and has a value of a maximum of 5% [38].

Due to the pressure delivered by VHU, the FHU pistons will press on the inclined disc with the forces F_1 and F_2, respectively, given by [39]:

$$F_1 = p_1 S \qquad F_2 = p_2 S, \tag{17}$$

where p_1 is the high pressure at the hydraulic fluid inlet in FHU, and p_2 is the low pressure at the fluid outlet from the FHU.

According to Newton's third law of dynamics, the reaction principle, the disc will act on the pistons with the same forces R_1, and R_2, respectively. From Figure 7, it can be seen that only the tangential component of the reaction forces at the surface of the disc, R_1'' and R_2'', will give a torque on the axis of the rotor of the FHU. But as $p_2 \ll p_1$, it is also obvious that $R_2'' \ll R_1''$, in which case only the torque created by the force R_1'' acting at arm x will be considered:

$$M_1 = R_1'' \cdot x = R_1'' \cdot \frac{D}{2} \sin \varphi = p_1 S \frac{D}{2} \text{tg } \gamma_m \sin \varphi. \tag{18}$$

This relationship shows that the motor torque varies sinusoidally with the rotation angle of the HM rotor.

If all torques produced by the N pistons are added together, the total instantaneous engine torque obtained will be:

$$M_t = \sum_1^N M_i = p_1 S \frac{D}{2} \text{tg } \gamma_m [\sin \varphi + \sin(\varphi + \frac{2\pi}{N}) + \sin(\varphi + 2\frac{2\pi}{N}) + \ldots + \sin(\varphi + k\frac{2\pi}{N}) + \ldots + \sin(\varphi + N\frac{2\pi}{N})]. \tag{19}$$

From Equation (19), it can be seen that the obtained torque has a pulsating character that can be reduced by choosing a minimum odd number of 7–9 pistons. In this case, the average value of the torque at a rotation angle of 360° is:

$$M_{av} = N M_{1,av} = \frac{N}{2\pi} \int_0^\pi p_1 S \frac{D}{2} \text{tg } \gamma_m \sin \varphi d\varphi = \frac{p_1 NSD \text{tg } \gamma_m}{2\pi}. \tag{20}$$

By removing p_1 from the Equations (15), (16) and (20) results:

$$\Omega_m = C_m (Q_p - K_p \cdot p_1) = C_m Q_p - C_m K_p \frac{M_{av}}{NSD \text{tg } \gamma_m / 2\pi} = C_m C_p \Omega_p \text{tg } \gamma - k_1 \cdot M_{av} = C \Omega_p \text{tg } \gamma - k_1 \cdot M_{av}, \tag{21}$$

where $C = C_m C_p$ and $k_1 = 2\pi C_m K_p / (NSD \text{tg } \gamma_m)$.

Analyzing Equation (21), it can be concluded that the mechanical characteristic of the CSD is linear with the control angle of the mobile disc and slightly falling depending on the value of the average torque. Also, the stiffness k_1 of the characteristic does not depend on the control angle γ.

3.2. Brushless Synchronous Generator (BSG)

Due to the advantages they have over other alternating current generators, like the highest electrical power per kilogram per rpm, lowest reactance, etc., the best regulation and performance under transient load conditions, the wound-pole, salient-pole synchronous generator is the most used electrical power source in an aircraft's EPS.

It started to be used in aviation at the beginning of the 20th century as a source of electrical energy for early gyroscope instruments [40], early communication systems (radiotelephone and radiotelegraph) [41] and early navigation systems (system of blind landing) [42], developed in WWI. At the end of the war, in order to increase the safety of passengers, it was introduced in commercial aviation under the name of high-frequency current generator, often driven by a wind turbine [40,41,43], because the power of the engine was quite small, hardly ensuring the lift of the aircraft, and also because its characteristic was not suitable for driving alternators.

Since the second decade of the 20th century, with the advances made by the aviation engine manufacturers in increasing the specific power of the engine, and also due to its reliability, a surplus of power has been created that was used to drive electric generators.

However, what actually led to the introduction of alternators as an aviation power source was the manufacture of the first constant speed hydraulic drive in 1946 by Sundstrand Machine Tool Co, as previously explained.

It is well known that the operational reliability and lifetime of an electric machine are determined by the following factors: the quality of the electrical insulation, the quality of the bearings and the reliability of the moving contacts (brushes and slip rings device). As the first two factors depend on the level of technology reached in those fields at that time, the third can be eliminated by using a synchronous generator without moving contacts. The most widely used solution for this, including in aviation since 1942, is the synchronous generator with brushless exciter, called the brushless synchronous generator (BSG), shown in Figure 8.

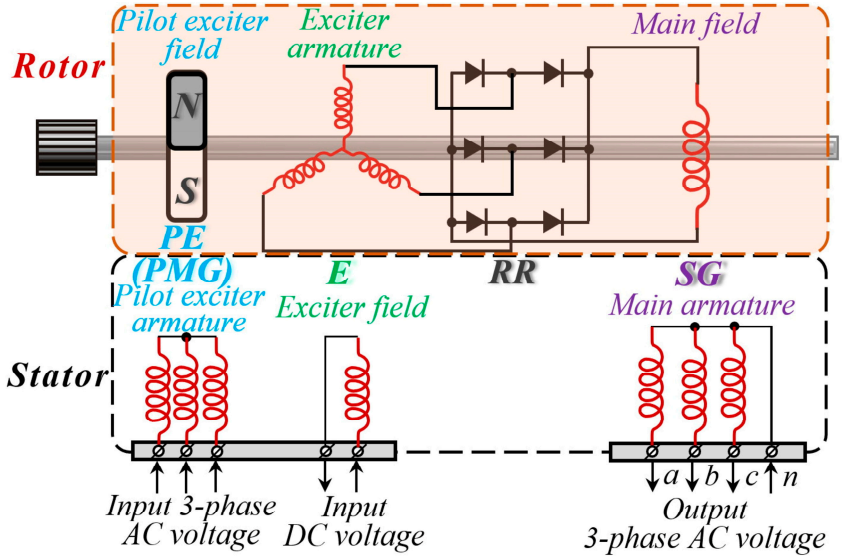

Figure 8. Components of a modern BSG [2]: *PE*—pilot exciter, a 3-ph *SG* with permanent magnet (*PMG*); *E*—exciter, a 3-ph *SG* of inverted construction; *RR*—rotary rectifier.

Presently, in the theory of synchronous machines, a few precise mathematical representations of synchronous generators are well defined and validated, but in this paper, only the representation per unit (p.u.) will be briefly presented.

For determining the equations of a synchronous machine, the following assumptions were made:

1. The stator windings are sinusoidally distributed along the air gap as long as mutual effects with the rotor are neglected;
2. The stator slots do not cause major variations in rotor inductances with rotor position;
3. The magnetic hysteresis is negligible;
4. The magnetic saturation effects are negligible;
5. The currents in the damper flow in two sets of closed circuits: one, whose flow is in line with that of the field along the *d*-axis, and the other, whose flow is at a right angle to the field axis or along the *q*-axis, as shown in Figure 9.

As the equations of a synchronous machine contain inductance terms, which vary with the angle θ, and with the time, an easier representation could be obtained by the transformation of stator variables, also known as the *dq0* transformation. The angle θ is the angle by which the *d*-axis leads the magnetic axis of phase *a* winding in the direction of rotor rotation, as shown in Figure 9 [2]:

$$\left.\begin{array}{c}\theta = \omega_r t \\ \omega_r = p\Omega_r \\ \Omega_r = \Omega = \Omega_{CSD}\end{array}\right\} \Longrightarrow \theta = p\Omega_r t, \quad (22)$$

where ω_r is the rotor angular speed (in electrical terms), Ω_r is the mechanical angular velocity (the speed, Ω, at which the SG is driven by the CSD with Ω_{CSD}), 2p is the number of poles. Using Park transformation, the stator's voltages, e_a, e_b, e_c, currents i_a, i_b, i_c and flux linkages ψ_a, ψ_b, ψ_c have to be transformed to dq rotor orthogonal coordinates and also, for p.u. representation, the variables must be normalized. In this case, the summary of SG equations in p.u. is [44]:

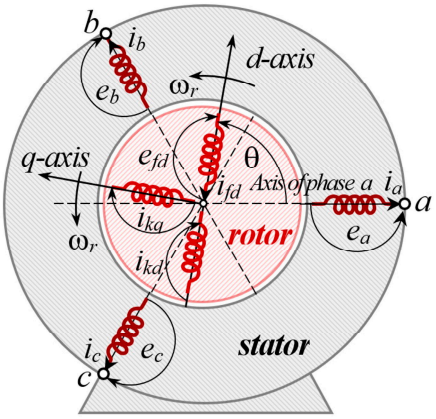

Figure 9. SG phase-variable circuit model [2]; *a*, *b*, *c*—stator phase windings; *fd*—field winding; *kd*—*d*-axis dumper circuit; *kq*—*q*-axis dumper circuit; *k* = 1, n, n—number pf dumper circuits; *θ*—angle by which *d*-axis leads the magnetic axis of phase *a* winding; ω_r—rotor angular speed.

p.u. stator voltage equations:

$$\begin{aligned} e_d &= \frac{1}{\omega_{base}}\frac{d\psi_d}{dt} - \psi_q\omega_r - R_a i_d \\ e_q &= \frac{1}{\omega_{base}}\frac{d\psi_q}{dt} + \psi_d\omega_r - R_a i_q \\ e_0 &= \frac{1}{\omega_{base}}\frac{d\psi_0}{dt} - R_a i_0, \end{aligned} \tag{23}$$

with R_a stator resistance.

p.u. rotor voltage equations:

$$\begin{aligned} e_{fd} &= \frac{1}{\omega_{base}}\frac{d\psi_{fd}}{dt} - R_{fd} i_{fd} \\ 0 &= \frac{1}{\omega_{base}}\frac{d\psi_{1d}}{dt} - R_{1d} i_{1d} \\ 0 &= \frac{1}{\omega_{base}}\frac{d\psi_{1q}}{dt} - R_{1q} i_{1q}, \end{aligned} \tag{24}$$

where R_{fd}, R_{1d} and R_{1q} are the resistance of the rotor field circuit, *d*-axis damper and *q*-axis for winding 1.

p.u. stator flux linkage equations:

$$\begin{aligned} \psi_d &= -(L_{ad} + L_l) i_d + L_{ad} i_{fd} + L_{ad} i_{1d} \\ \psi_q &= -(L_{aq} + L_l) i_q + L_{aq} i_{1q} \\ \psi_0 &= -L_0 i_0 \end{aligned} \quad , \tag{25}$$

with L_l the stator leakage inductance, L_{ad} and L_{aq} are the mutual inductances of stator *d*-axis and *q*-axis.

p.u. rotor flux linkage equations:

$$\begin{aligned} \psi_{fd} &= L_{ffd} i_{fd} + L_{f1d} i_{1d} + L_{ad} i_d \\ \psi_{1d} &= L_{f1d} i_{fd} + L_{11d} i_{1d} - L_{ad} i_d \\ \psi_{1q} &= L_{11q} i_{1q} - L_{aq} i_q \end{aligned} \quad , \tag{26}$$

where L_{ffd} is the self-inductance of the rotor field circuit, L_{11d} and L_{11q} are the self-inductance of the d-axis damper, respectively, q-axis damping for winding 1, L_{f1d} is the rotor field circuit and d-axis damper winding 1 mutual inductance.

3.3. Control of the IDGS

In order for an EPS to be able to operate onboard the aircraft, its qualitative parameters must strictly fit within the values regulated by several standards [45,46]. For an AC one, the most important of these are voltage and frequency.

As, in such a system, the electricity is generated by means of a BSG (i.e., a synchronous generator), the frequency of which depends on the speed of rotation with which it is driven by the CSD, n, but also on the load, I_G, it must first be controlled in frequency.

3.3.1. Automatic Frequency Regulator (AFR)

Frequency regulation is achieved by rotational speed using the CSD, as carried out by Sundstrand, since the introduction of this system in 1946, or more recently by electronic frequency converters. Given that, currently, 90.69% of commercial aircraft in service use the CSCF configuration (as shown in Figure 2), this paragraph will present the rotational speed regulation using a rotational speed regulator (RSR) or governor system, as shown in Figure 5.

In order to be able to develop the mathematical model of such a regulator, its mode of operation must first be explained.

If the rotation speed of the generator is a rated one, then the force measured by the centrifugal transducer 1, along the distributor 2, is balanced by the elastic force of the spring 3, the distributor remaining in the middle position blocking the access of the liquid under pressure from actuator 5. If the rotational speed is different from the nominal one, the centrifugal transducer 1 will move the distributor 2 to the left or right as the rotational speed decreases or increases, thus allowing for the circulation of the liquid under pressure to the left or right of the actuator's piston 5, moving the angle of the CSD's control device by $\gamma \pm \Delta\gamma$. For the qualitative study of the RSR regulation process, its components (the centrifugal transducer (measuring device), the hydraulic servomotor (control device) and the controlled object (CSD and BSG, i.e., IDG)), as represented in Figure 10, will be studied.

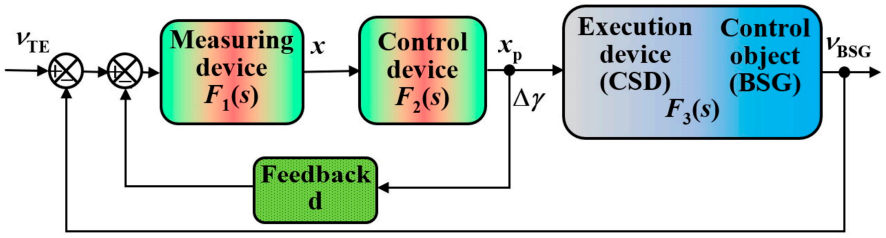

Figure 10. The RSR diagram [2].

For the centrifugal transducer, or measuring device, at a position corresponding to the nominal rotational speed of the BSG and at a fixed position of the distributor shaft, Newton's second law, the action principle, gives:

$$\mathrm{m}\frac{d^2x}{dt^2} = \sum_{i=1}^{4} F_i \,, \tag{27}$$

with: x is the displacement of the distributor shaft, m the mass of the moving parts relative to the distributor shaft and F_i the four forces that act on the shaft: the centrifugal force F_c, the elastic force of the spring F_s, the dry friction force F_{fd} and the friction viscous force F_{fv}.

Since the viscous friction force is proportional to the shaft speed, and the dry friction force is much smaller than the other forces acting on the distributor shaft, Equation (27) becomes:

$$\mathrm{m}\frac{d^2x}{dt^2} + \mathrm{k_f}\frac{dx}{dt} + F_s(x) \ = F_c(\omega, x), \tag{28}$$

where $\mathrm{k_f}$ is the coefficient of dry friction.

As Equation (28) is non-linear due to the non-linear character of the centrifugal force, the behavior for small deviations from the steady-state operating condition, i.e., its specific point of regulation (POR), will be studied, in order to linearize it:

$$\mathrm{m}\frac{d^2\Delta x}{d\Delta t^2} + \mathrm{k_f}\frac{d\Delta x}{d\Delta t} + \Delta F_s(x) = \Delta F_s(\omega, x), \tag{29}$$

equivalent with

$$\mathrm{m}\frac{d^2\Delta x}{d\Delta t^2} + \mathrm{k_f}\frac{\mathrm{d}\Delta x}{d\Delta t} + \left.\frac{\partial F_s}{\partial x}\right|_{x_0}\Delta x = \left.\frac{\partial F_c}{\partial \omega}\right|_{\omega_0}\Delta\omega + \left.\frac{\partial F_c}{\partial x}\right|_{x_0}\Delta x. \tag{30}$$

Further transforming Equation (30) into an operational form and then dividing by a stabilized reference quantity yields the dimensionless variables:

$$\left\{\mathrm{m}\cdot s^2 + \mathrm{k_f}\cdot s + \left[\left.\frac{\partial F_s}{\partial x}\right|_{\mathrm{x_0}} - \left.\frac{\partial F_c}{\partial x}\right|_{\mathrm{x_0}}\right]\right\}\Delta X = \left.\frac{\partial F_c}{\partial \omega}\right|_{\omega_0}\Delta\Omega\Bigg| \div F_0 \tag{31}$$

$$\left\{\mathrm{m}\cdot s^2 + \mathrm{k_f}\cdot s + \left[\left.\frac{\partial F_s}{\partial x}\right|_{\mathrm{x_0}} - \left.\frac{\partial F_c}{\partial x}\right|_{\mathrm{x_0}}\right]\right\}\frac{\mathrm{X_0}}{\mathrm{F_0}}\frac{\Delta X}{\mathrm{X_0}} = \left.\frac{\partial F_c}{\partial \omega}\right|_{\omega_0}\frac{\Omega_0}{\mathrm{F_0}}\frac{\Delta X}{\Omega_0}. \tag{32}$$

Expressing with $x = \Delta X/\mathrm{X_0}$, the relative displacement of the distributor shaft, $\nu = \Delta\Omega/\Omega_0$ the relative variation of the angular velocity of the regulator shaft and the corresponding constants, Equation (32) becomes:

$$(T_\mathrm{c}\cdot s^2 + T_\mathrm{v}\cdot s + \mathrm{k_s})x = \mathrm{K}\nu. \tag{33}$$

Given that for $\mathrm{T_c} \ll \mathrm{T_v}$, the time constant of the centrifugal transducer can be neglected, then Equation (33) becomes:

$$(T_1\cdot s + 1)x = \mathrm{K_1}\nu, \tag{34}$$

with the transfer function of the centrifugal transducer given by:

$$F_1(s) = \frac{x(s)}{\nu(s)} = \frac{\mathrm{K_1}}{T_1\cdot s+1}. \tag{35}$$

To determine the equation of motion of the control device, the actuator, the input quantity x, the displacement of the distributor piston, and the output displacement x_p of the actuator piston as the output quantity are considered. As the input and output quantities are one-dimensional, it can be considered that the hydraulic actuator is a hydraulic amplifier. Considering that the volume flow of the liquid circulating in the channels of the regulation system is proportional to the access sectional areas and to the second-order radical of the pressure drops between the outlet and the inlet channels, then:

$$\mathrm{S_p}\frac{\mathrm{d}x_\mathrm{p}}{\mathrm{d}t} = \mathrm{aS_d}\sqrt{p_0}\,, \tag{36}$$

where $\mathrm{S_p}$ is the area of the servomotor piston, $\mathrm{S_d}$ is the area of the distributor passage hole, p_0 the pressure drops of the hydraulic fluid in the channels and a is a proportionality

coefficient. Given that the distributor has no dead zones when operating, it can be assumed that the displacement speed of the piston is proportional to the displacement, x, i.e.:

$$\frac{\mathrm{d}x_\mathrm{p}}{\mathrm{d}t} = f(x) = \mathrm{k_p}x. \tag{37}$$

As the passage section of the distributor $\mathrm{S_d}$ is proportional to its displacement, x, then:

$$\mathrm{S_d} = \mathrm{k_d}x, \tag{38}$$

and Equation (36) becomes:

$$\mathrm{S_p}\frac{\mathrm{d}x_\mathrm{p}}{\mathrm{d}t} = \mathrm{ak_d}x\sqrt{p_0}. \tag{39}$$

To determine the equation of motion of the servomotor, the transfer function, the same procedure as in the first case is applied, obtaining:

$$\begin{gathered} \mathrm{S_pX_{p_0}}s\frac{\Delta X_\mathrm{p}(s)}{\mathrm{X}_{p_0}} = \mathrm{a}\sqrt{p_0}\mathrm{k_d}\mathrm{X_0}\frac{\Delta X(s)}{\mathrm{X_0}} \\ T_2 s x_\mathrm{p}(s) = \mathrm{K}_2 x(s) \\ F_2(s) = \frac{x_\mathrm{p}(s)}{x(s)} = \frac{\mathrm{K}_2}{s\cdot T_2}, \end{gathered} \tag{40}$$

where $x_\mathrm{p}(s) = \Delta X_\mathrm{p}(s)/\mathrm{X_{p0}}$ is the relative variation in the actuator piston displacement, $\mathrm{T_2} = \mathrm{S_pX_{p0}}$ is the time constant of servomotor and $\mathrm{K_2} = \mathrm{a}\sqrt{p_0}\mathrm{k_d}\mathrm{X_0}$ is the constant of proportionality.

The equation of the controlled object can be determined by considering the steady-state operation of a BSG driven by the aircraft turbofan engine, as represented in Figure 11, by applying Newton's second law regarding the drive shaft:

$$\mathrm{J}\frac{d\Omega}{dt} = M_1 - M_2. \tag{41}$$

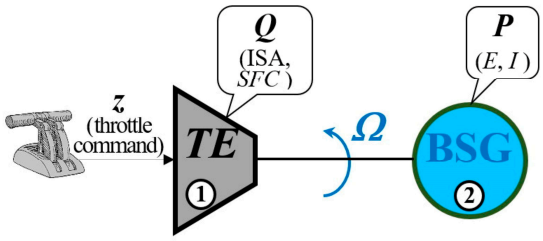

Figure 11. Diagram of the driven generator model [2].

The TE torque, M_1, depends on the angular velocity, Ω, command (i.e., throttle command), z, and disturbance (given by international standard atmosphere (ISA) and specific fuel consumption (SFC)), Q:

$$M_1 = M_1(\Omega, z, Q), \tag{42}$$

and the torque of the BSG, M_2, depends on electromagnetic power (i.e., the electromotive force E and loads current I), P, and mechanical angular velocity, Ω:

$$M_2 = M_2(\Omega, P). \tag{43}$$

Applying the same procedure as in the previous cases, by disturbing the steady-state operating condition with small deviations, respectively, results in:

$$\mathrm{J}\frac{d\Delta\Omega}{d\Delta t} = \Delta M_1 - \Delta M_2, \tag{44}$$

equivalent with:

$$\mathrm{J}\frac{d\Delta\Omega}{d\Delta t}+\frac{\partial M_2}{\partial\Omega}\Delta\Omega+\frac{\partial M_2}{\partial P}\Delta P=\frac{\partial M_1}{\partial\Omega}\Delta\Omega+\frac{\partial M_1}{\partial z}\Delta z+\frac{\partial M_1}{\partial Q}\Delta Q, \tag{45}$$

or:

$$\mathrm{J}\frac{d\Delta\Omega}{d\Delta t}+\left[\frac{\partial M_2}{\partial\Omega}-\frac{\partial M_1}{\partial\Omega}\right]\Delta\Omega=\frac{\partial M_1}{\partial z}\Delta z+\frac{\partial M_1}{\partial Q}\Delta Q-\frac{\partial M_2}{\partial P}\Delta P. \tag{46}$$

Transforming Equation (46) into dimensionless variables by dividing it with the stabilized torque M_0 made it operational by using the Laplace transform and expressing with $\nu = \Delta\Omega/\Omega_0$ (called the relative variation of the driven mechanical angular velocity), $\sigma = \Delta z/\mathrm{z}_0$ (the relative variation of the aircraft turbofan engine command, which in this case is even $x(s)$), $q = \Delta Q/\mathrm{Q}_0$ (the relative variation of the disturbance acting on the aircraft turbofan engine), $p_\mathrm{e} = \Delta P/\mathrm{P}_0$ (the relative variation of the electromagnetic power of the generator) and the respective constants results in [42]:

$$Ts\nu(s)+\mathrm{S}\cdot\nu(s)=\mathrm{N}\cdot\sigma(s)+\lambda\cdot\mathrm{q}(s)-p_e(s). \tag{47}$$

As the variation in the electromagnetic power is small compared to the other quantities, $p_\mathrm{e}(s) \cong 0$, and due to the CSD, the variations of the disturbances at the aircraft turbofan engine are approximately zero, $q \cong 0''$, so Equation (47) becomes:

$$(\mathrm{T}s+\mathrm{S})\nu(s)=\mathrm{N}\cdot\sigma(s), \tag{48}$$

having the transfer function:

$$F_3(s)=\frac{\nu(s)}{\sigma(\mathrm{s})}=\frac{\nu(s)}{x(s)}=\frac{\mathrm{N}}{\mathrm{T}\cdot s+\mathrm{S}}=\frac{\mathrm{N}'}{\mathrm{T}'\cdot s+1}. \tag{49}$$

Finally, having all the transfer functions of the system components, according to the block diagram in Figure 10, the transfer function of the regulating system is [47]:

$$F(s)=\frac{\mathrm{K}}{T_1T_2'T_M's^3+(T_1T_2'+T_2'T'_M)s^2+(T_2'+T_M')s+1+\mathrm{K}'}, \tag{50}$$

where $\mathrm{K}=\mathrm{K}'_{12}\mathrm{N}'$, $\mathrm{K}'_{12}=1/\mathrm{d}$ and $T_2'=T_2/(\mathrm{d}\cdot\mathrm{K}_1\cdot\mathrm{K}_2)$.

3.3.2. Automatic Voltage Regulator (AVR)

It is well known that the voltage at the aircraft buss bar with the limits regulated by the ISO 1540:2006 standard [45] is given by the precise operation of the synchronous machines, which largely depends on the exact design of its excitation system but also on the voltage transducer and the regulator of voltage. To help the manufacturers of electric machines, but also the manufacturers of components, the IEEE society developed the standard IEEE Std 421.5 [48] in which models for the excitation system of synchronous generators, as well as models for their control, were included. Thus, the general functional block diagram of a synchronous machine, shown in Figure 12, is composed of the following subsystems: a terminal voltage transducer, an exciter system, an automatic voltage regulator and a protection device. Models for all these subsystems are presented in the recommended practice of the standard. As seen in Figure 12, the subsystem for the frequency regulator and the subsystems that are included in the system used to control the BSG, namely the generator control unit (GCU), are also represented.

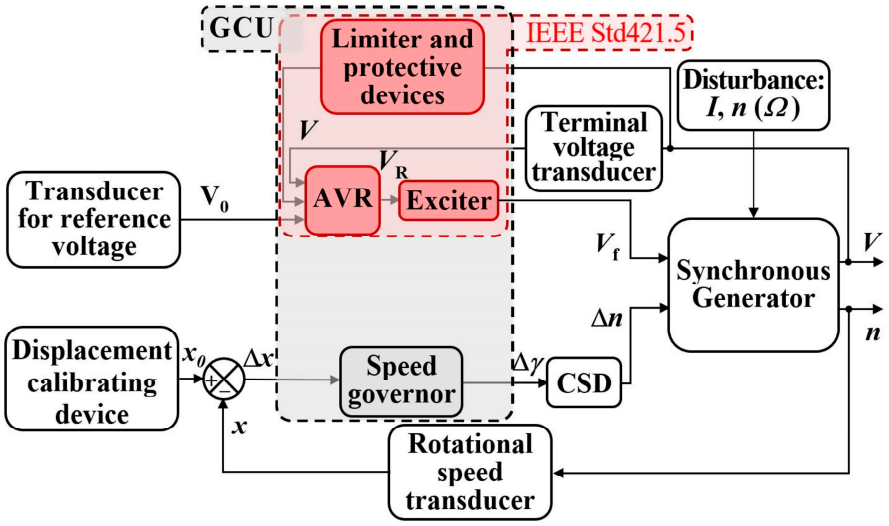

Figure 12. The control of a BSG [2,48].

From IEEE Std 421.5, three distinct types of excitation are identified for the exciter:

- Type DC, which uses a DC generator as the source of direct current for the BSG field;
- Type AC, using an AC generator and a stationary or rotating rectifier to obtain the direct current;
- Type ST (static), in which excitation current is supplied by using transformers or auxiliary generator windings and rectifiers.

As all generators powering the aircraft in service are based on Westinghouse's company (Pittsburgh, PA, USA) generator [49], according to [48], the recommended excitation mode is the AC1A type. The model of this type of exciter is shown in Figure 13, where the parameters are: the normalized load current of the exciter I_N; the load factor of the rectifier F_{EX}, which is a function of I_N; the field current of the synchronous machine I_f; the reverse switching reactance of the exciter voltage V_E; the error signal voltage V_{err}; the exciter's output voltage V_f; the excitation system stabilizer's output V_F; the terminal voltage V; the voltage regulator's output V_R; the voltage regulator time constants T_A, T_B, and T_C; the exciter time constant T_E; the time constant of filter damping T_F; the voltage regulator gain K_A; the rectifier load factor K_C; the demagnetization factor K_D; the exciter's constant K_E; the damping filter gain K_F; and the exciter's saturation function S_E.

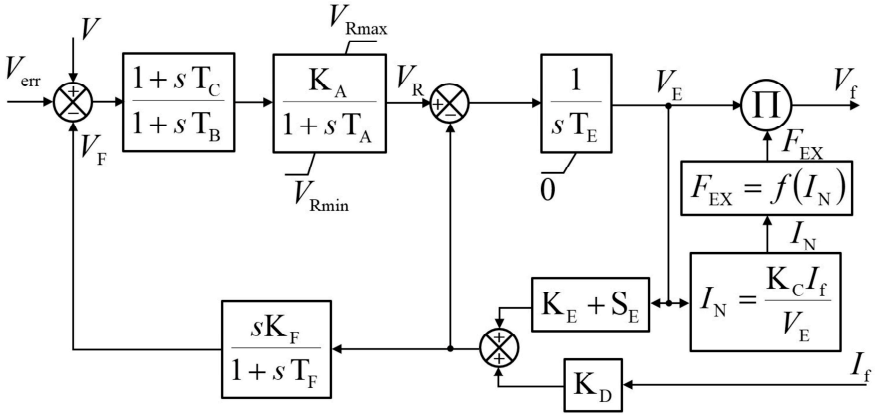

Figure 13. Type AC1A alternator rectifier excitation system with noncontrolled rectifiers and feedback from exciter field current [48].

4. Simulation and Results

The B737-800, the subject of this paper's simulation, is part of the next-generation version. Since its launch in late 1996, 6900 units have been produced [50], of which 5620 are still flying in the world's fleets today [51].

To validate the Simulink model of the EPS, the power generation and distribution system of the B737-800 aircraft was developed, as shown in Figure 14. The system is composed of the CFM56-7B26 turbofan engine model, the IDGS model, the GCU model, which has the role of regulating the voltage using BSG excitation and the frequency with the CSD, and the last block, the secondary electrical distribution model with its loads, two three-phase active loads of 25 kW each, and one DC load of 2.8 kW fed by two transformer rectifier units (TRUs) of 2.1 kW each. Also, the model has a control panel used to control and measure the systems (the turbofan engine, IDGS and loads).

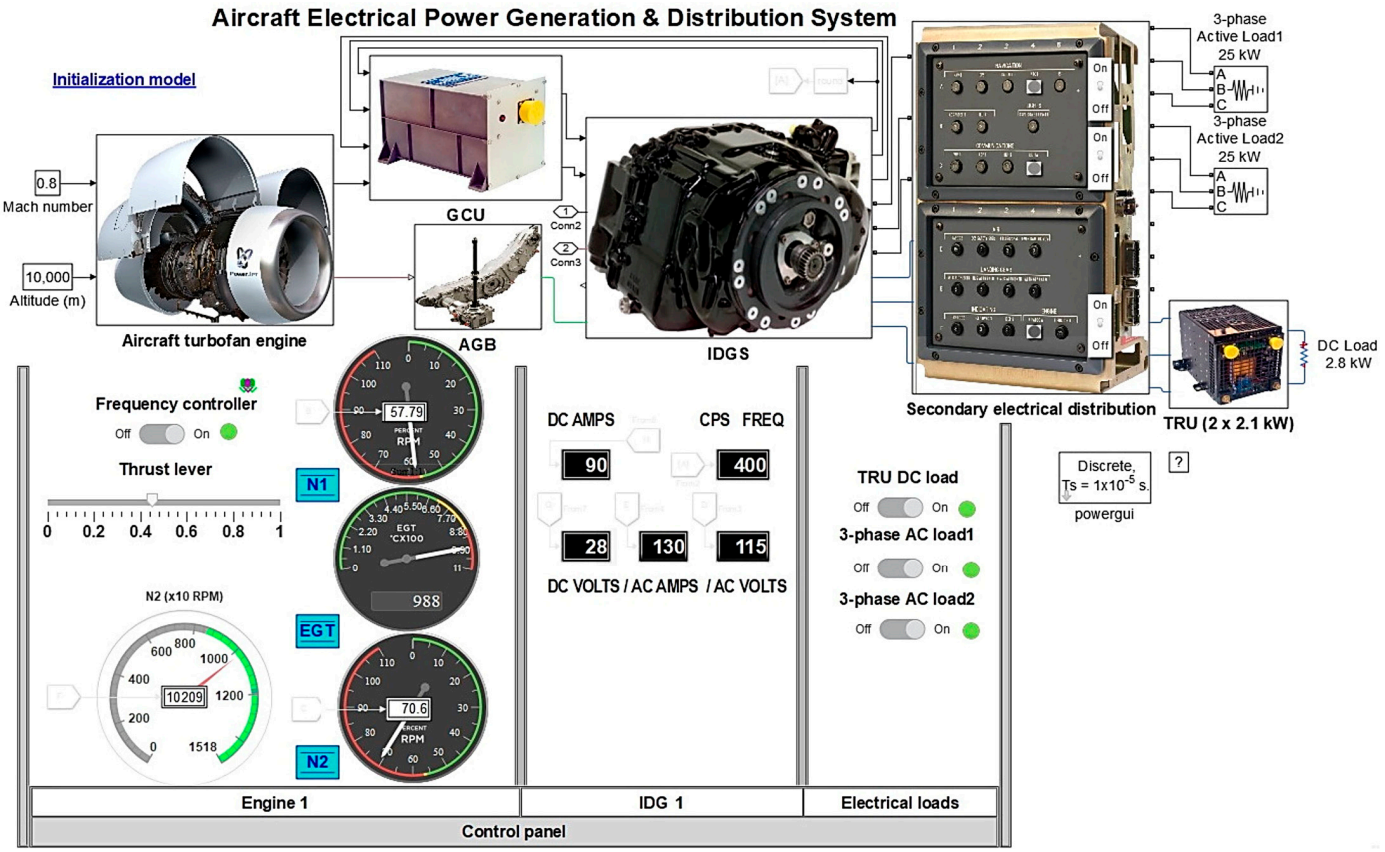

Figure 14. Aircraft electrical power generation and distribution system Simulink model.

This subject has been studied before in the specialized literature using Matlab/Simulink [1,2,52,53] or simulations in other programming languages (Sabre [54,55], ANSYS Simplorer [56,57], Amesim [58], SimVimCockpit [59]), but, in all these cases, the generator was driven directly from a constant torque. None of these models simulated the actual case of an aircraft's electrical system operation, i.e., using a model of an aircraft engine that first drives the CSD and then, in turn, drives the IDG. There was one exception, the case where, although the CSD was implemented, it was operated again by a constant torque and not by an aircraft engine model [2].

The model of the electrical power generation and distribution system of the B737-800 aircraft was made in Simulink v 8.7/Matlab v.9.0.

Three simulation scenarios for operating the EPS were developed, dedicated to the following phases of the flight mission [60]:

- En route (ENR);

- Ground Operation and Loading (GOL);
- Initial climb (ICL).

In the next step, these three scenarios will be analyzed, starting with the first scenario, the En route. This is the longest from the terms from an operating time point of view, and it can have many variations in the electrical system loading; it will use only three examples, by starting operation with the three electric loads. For the other two scenarios, due to their small operating times, the loading will be considered as constant at the value mentioned below.

4.1. Simulation of the En Route Scenario

According to [60], cruising is the longest phase in flight from an aircraft's mission, in which the EPS can be loaded somewhere in the range 30–100%

The general flight conditions under which this simulation is performed for this phase are as follows:

- Altitude: 10,000 m;
- Mach number: 0.8;
- Command of the turbofan engine by means of the thrust lever: 0.4408;
- Real operation time of aircraft in this scenario: 207 min out of a total mission flight time of 322 min [47].

4.1.1. Turbofan Engine Simulink Model

Since Equation (11) for determining the force of a jet engine is not practical but also out of reach (lack of parameters, or the impossibility of measuring them with sensors), engine specialists [61] and academic researchers [62,63] together with international specialized agencies (EUROCONTROL (Brussels, Belgium) with its Base of Aircraft Data (BADA) project [64]) have determined a simpler and more accessible mathematical model so that research and simulations can be done in the field.

According to this reduced model, the thrust of a turbofan engine can be expressed as [62]:

$$T = \tau \cdot T_0. \tag{51}$$

In Equation (51), T_0 is the sea-level static dry thrust, which is always known, and τ, a factor depending on a series of experimental factors, Mach number, M, and the bypass ratio, BPR, thus:

For $0 < M \leq 0.9$

$$\tau \cdot = F_\tau[K_{1\tau} + K_{2\tau} + (K_{3\tau} + K_{4\tau} \cdot BPR)\, M)]\ \sigma^s. \tag{52}$$

For $M > 0.9$

$$\tau \cdot = F_\tau[K_{1\tau} + K_{2\tau} + (K_{3\tau} + K_{4\tau} \cdot BPR)\, (M - 0.9)]\ \sigma^s. \tag{53}$$

where F_τ is a factor used for afterburning (equal to unity under basic, dry operating conditions), $K_{1\tau}$, $K_{2\tau}$, $K_{3\tau}$ and $K_{4\tau}$ factors are given in Table 1; factor s, depending on altitude, and $\sigma = \rho/\rho_0$ is relative density, with ρ_0 density at sea level for ISA conditions.

To increase the accuracy of Equation (51), a correction is introduced as a function of the static pressure at the flight level [61]:

$$T_{\,corrected} = T/\delta, \tag{54}$$

where $\delta = p/p_0$ is the ratio of the static pressure, with p_0 pressure at sea level for ISA conditions.

From Figure 14, it can be seen that the output of the turbofan engine is linked to the accessory gearbox, AGB, which in turn drives the IDGS; therefore it is a matter of a rotational speed, which is generally the rotational speed of the high-pressure rotor, also called core rotational speed, N_2.

Table 1. Turbofan engine thrust parameters (data from [61]).

Bypass Ratio BPR	Mach Number Range M	Operating Condition	$K_{1\tau}$	$K_{2\tau}$	$K_{3\tau}$	$K_{4\tau}$	s *
1 or lower	0–0.4	Dry	1.00	0	−0.2	0.07	0.8
		Wet	1.32	0.062	−0.13	−0.27	0.8
	0.4–0.9	Dry	0.856	0.062	0.16	−0.23	0.8
		Wet	1.17	−0.120	0.25	−0.17	0.8
	0.9–2.2	Dry	1.00	−0.145	0.5	− 0.05	0.8
		Wet	1.40	0.03	0.8	0.4	0.8
3 to 6	0–0.4	Dry	1.0	0	−0.6	−0.04	0.7
	0.4–0.9	Dry	0.88	−0.016	−0.3	0	0.7
8	0–0.4	Dry	1.0	0	−0.595	−0.03	0.7
	0.4–0.9	Dry	0.89	−0.014	−0.3	0.005	0.7

* s coefficient values must be applied up to 11 km altitude, above witch its value is unity.

As stated in Section 2, the accurate determination of engine thrust is very important because it is basically the force that keeps the airplane in the air. Unfortunately, both the determinations of the thrust force, the exact formula, and the approximate one determined above assume parameters that are difficult to measure onboard the aircraft, so to be able to measure it, indirect methods of measurement must be used. Considering that the easiest parameters to measure onboard are temperature and rotational speed, the aircraft engine manufacturers give the dependence between the thrust and the low-pressure rotor rotational speed, also called fan rotational speed, N_1, and the thrust and the exhaust gas temperature, EGT, respectively, in their characteristics. Thus, for the B737-800 aircraft engine, CFM56-7B26, the dependence between thrust and fan rotational speed N_1 is given in Table 2 [65].

Table 2. Dependence between traction and fan rotational speed N_1.

Nr. crt (1)	T [kN] (2)	N_1 [%] (3)	N_1 [rpm] (4 = 3 × $N_{1,100\%}$)	Nr. crt (1)	T [kN] (2)	N_1 [%] (3)	N_1 [rpm] (4 = 3 × $N_{1,100\%}$)	Nr. crt (1)	T [kN] (2)	N_1 [%] (3)	N_1 [rpm] (4 = 3 × $N_{1,100\%}$)
1	6.805	30	1552.5	6	25.780	55	2846.25	11	64.944	80	4140
2	10.186	35	1811.25	7	31.137	60	3105	12	76.731	85	4398.75
3	13.589	40	2070	8	37.809	65	3363.75	13	90.187	90	4657.5
4	17.259	45	2328.75	9	45.371	70	3622.5	14	104.533	95	4916.25
5	21.307	50	2587.5	10	54.491	75	3881.25	15	115.654	103.5	5356.12

Other parameters used for model development in Simulink are [66]:

- Maximum take-off Thrust: 11,699 daN;
- Maximum Exhaust Gas Temperature (EGT): 950 °C + 30 °C;
- Low-pressure rotor rotational speed ($N_{1,100\%}$): 5175 rpm;
- High-pressure rotor rotational speed ($N_{2,100\%}$): 14,460 rpm.

From [67], where the author in collaboration with the technical department of Turkish Airlines had access to the data of 51 different types of CFM56-7B turbo engines, the following relationships were extracted:

$$EGT = 495.1391 + 0.24703 \times N_1, \tag{55}$$

$$EGT = -11.6367 + 0.122011 \times N_2, \text{ respectively.} \tag{56}$$

From Equations (55) and (56), the dependence between the fan rotational speed N_1 and the core rotational speed N_2 results in:

$$N_2 = \frac{506.7758 + 0.24703 N_1}{0.122011}. \tag{57}$$

From Figure 15, it can be seen that the model has three inputs: the command of the airplane engine through the thrust lever, and the two parameters specific to the evolution of the airplane, altitude and speed (Mach number), and one output, the angular velocity of the core Ω_2.

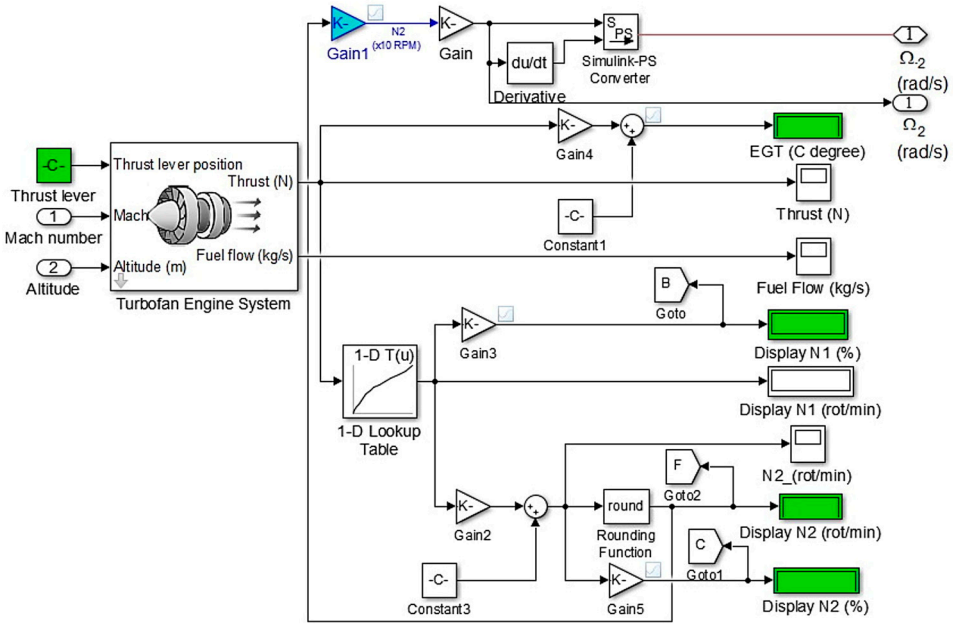

Figure 15. Simulink model for aircraft turbofan engine.

The three inputs that act on the dedicated block from the Simulink's Aerospace Blockset library, that actually implement Equations (51)–(54), give as output the thrust force, an irrelevant parameter in the IDGS's operation. Thus, it was implemented in Table 2 through the block "1- D Lockup table" as well as Equation (57), which resulted in the desired output. The background of the turbofan engine command and the parameters monitored in the "Control panel" are colored with green.

Following the simulation of the model shown in Figure 14 over a time interval of 35 s with the specified inputs and at a fixed thrust lever command at the 0.44 position, the thrust variation graph over time, the rotational speed of the fan N_1 and the rotational speed of the core N_2, respectively, were obtained, as shown in Figure 16. Although the two rotors of the turbofan engine, the low-pressure one and the high-pressure one, move independently, from Equation (57), but more obviously from Figure 16, it can be seen that the two shapes are proportional with a scale factor of $\frac{0.24703}{0.122011} = 2.02$. The parameters of the turbofan engine reach the steady state in about 10 s, which can be considered the time for the warm-up stage.

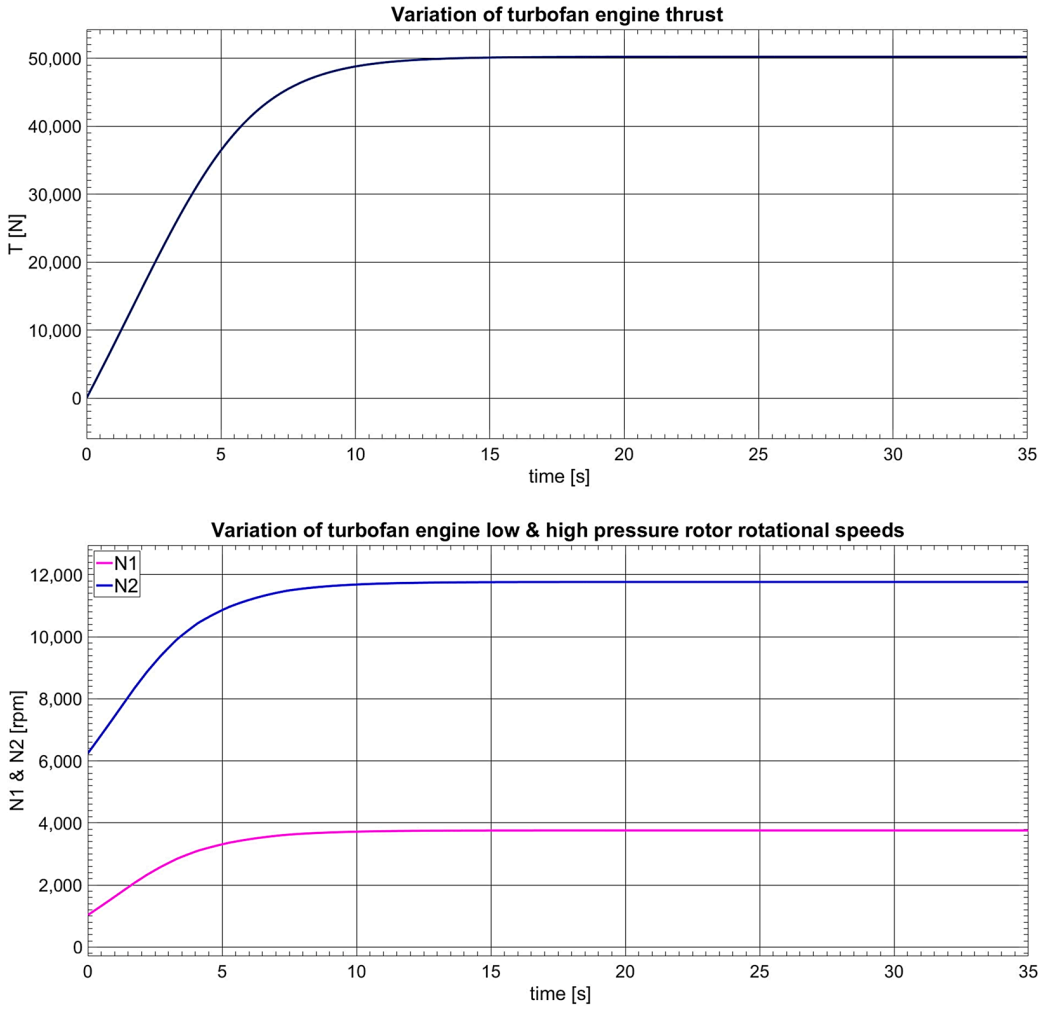

Figure 16. Variation of the aircraft turbofan engine characteristics.

4.1.2. Accessory Gearbox Simulink Model

The model is shown in Figure 17, which is practically a gear mechanism with a reduction ratio of 0.565 [66].

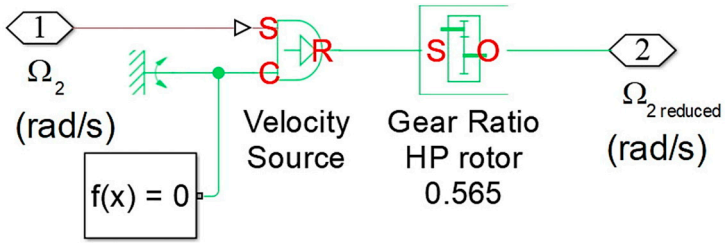

Figure 17. Simulink model for accessory gearbox.

Obviously, the output characteristic, expressed by $\Omega_{2\,\text{reduced}}$, plotted in Figure 18, is proportional to the input, the angular velocity of the core Ω_2, with a scale factor of 0.565.

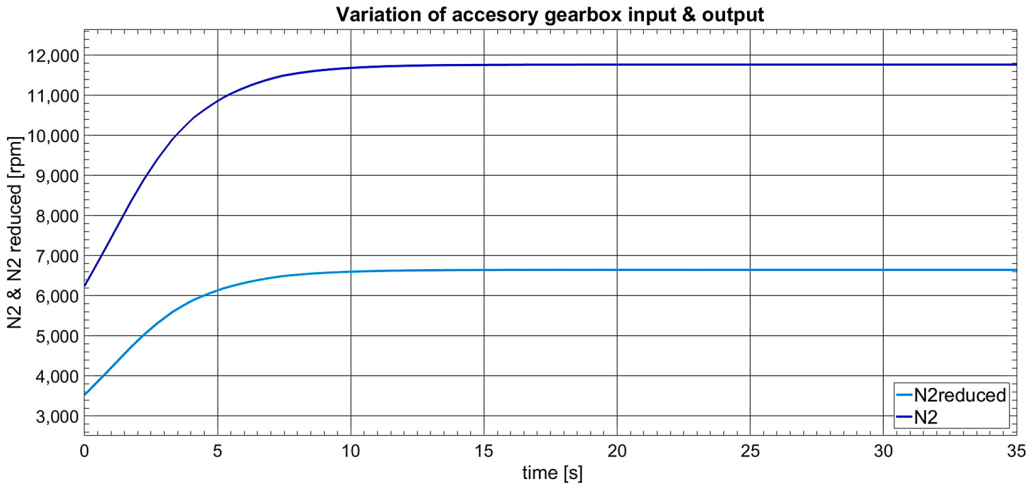

Figure 18. Variation of the accessory gearbox characteristics.

4.1.3. Integrated Drive Generator System Simulink Model

As stated in Section 3, and also presented in Figure 19, the model includes two components: the CSD and the BSG.

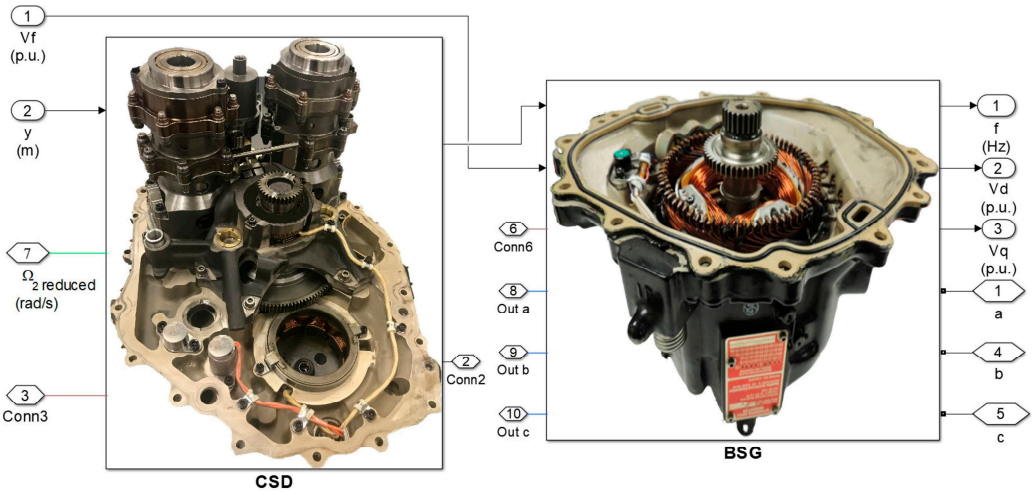

Figure 19. Simulink model for IDGS.

Constant Speed Drive Simulink Model

The CSD model consists of the updated Simulink axial-piston pump model "Hydraulic Axial-Piston Pump with Load-Sensing and Pressure-Limiting Control" [68] to nine pistons, a hydraulic motor with a linear hydraulic resistance and a lookup table with the values of the swashplate displacement included in the generator control unit (GCU) block.

According to the patents of Hamilton Sundstrand, the manufacturer of the CSD on the B737-800 aircraft [69–72], the simulation parameters for the CSD are listed in Figure 20 and the Simulink model of the CSD in Figure 21.

The parameters shown in Figure 20 are initialized by pressing the "Initialization model" square at the beginning of the simulation. The model has as input the reduced angular velocity, Ω_2, and as output, the output rotational speed of the CSD that drives the BSG and which, according to the prescriptions, must have a value of 24,000 rpm. The second input of the model is the swashplate displacement, y, which, according to the device's operation presented in Section 3.1, has the role of increasing or decreasing the input rotational speed so that the output remains constant at 24,000 rpm.

MATLAB Workspace Page 1
Sep 6, 2024 5:44:43 PM

Name	Value
act_arm	0.0320
actuator_init_pos	1.0000e-03
actuator_stroke	0.0080
carryover_angle	0.1222
f	*1x1 Figure*
hydraulic_fluid	'MIL-F-87257'
number_pistons	9
opts	*1x1 struct*
orifice_diameter	1.0000e-03
p4	'on'
p7	'off'
piston_area	1.0710e-04
piston_stroke	0.0220
pitch_radius	0.0058
Tfuse	0.1000
tr_slot_angle	0.0347
tr_slot_area	1.0000e-06
Ts	1.0000e-05
viscous_friction_coefficient	14

Figure 20. The Simulink model parameters.

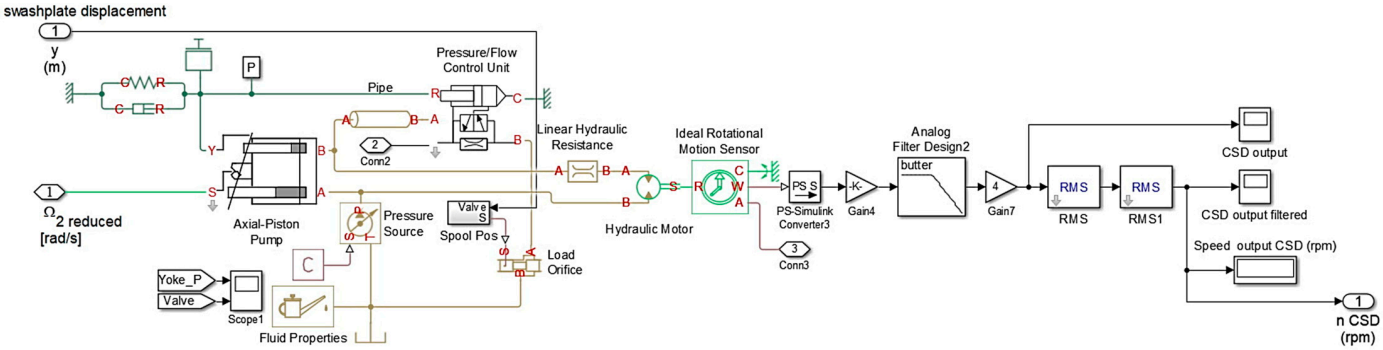

Figure 21. Simulink model for CSD.

Therefore, the next step was to find the correspondence between the y- swashplate displacement and the input rotational speed, which was practically shown extensively in [1] by testing a CSD model. From Equations (13) and (21), respectively, the swashplate displacement is proportional to the rotational speed through the angle γ, and a PID controller was developed in the GCU model using the "n-D Lookup Table" block from Simulink based on the linear interpolation operation.

Since the equations describing the dynamics of the "hydraulic motor" block and Simulink axial-piston pump model [68] are written under ideal conditions, for simulating the inherent hydraulic leakages that occur in the two hydraulic machines and the corresponding hydraulic circuit (pipes), and to obtain the slightly falling linear mechanical characteristic of the CSD from Equation (21), a linear hydraulic resistance was introduced before the hydraulic motor block. The characteristics of the CSD model obtained with the frequency controller disabled are shown in Figure 22.

It can be seen that the CSD's output rotation speed is 24,000 rpm, N_{CSD} = 24,000 rpm, reaches steady state in about 10 s, as the input (the output tracks the input), and the shape is pulsating and slightly decreasing.

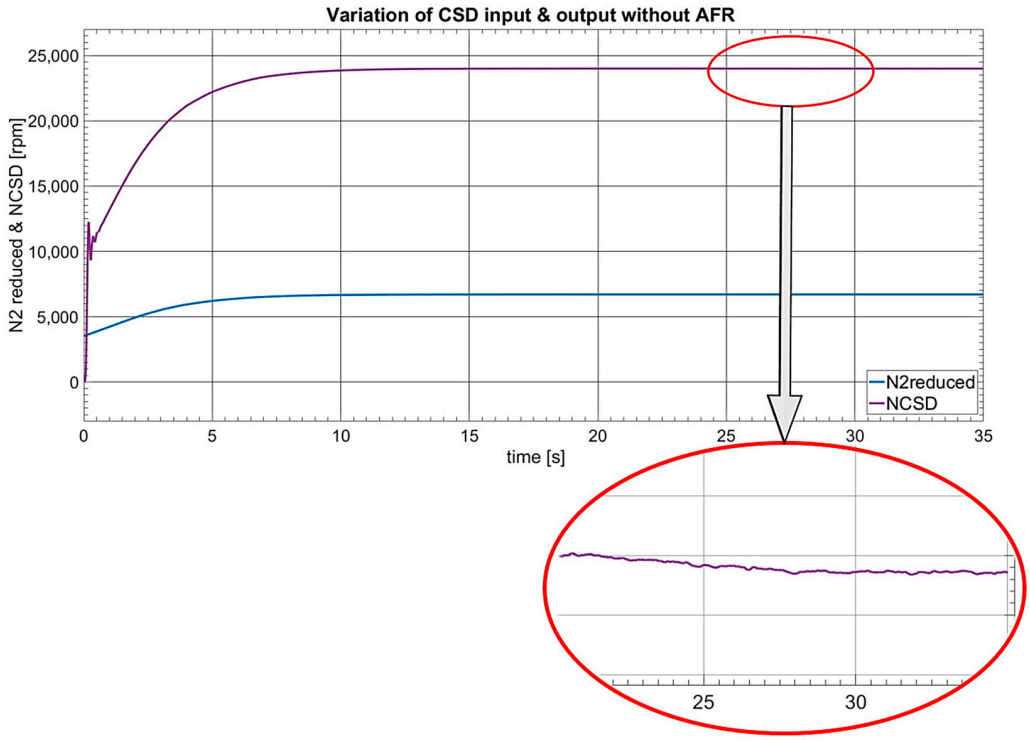

Figure 22. Variation of the CSD characteristics without AFR.

To more precisely demonstrate the CSD's mechanical characteristic, i.e., Equation (21), Figure 23 represent the simulation of the output of the CSD Simulink model with the frequency controller disabled, with an input that was not given by the turbofan engine model, due to its dynamics, but a constant torque with the value set once to the minimum, $N_{2min,reduced}$ = 4630 rpm, then at the value at which the simulations of this paper were made $N_{2reduced}$ = 6648 rpm.

As stated previously in [1] and demonstrated once more in this simulation, the pulsating effect due to the hydraulic pump pistons can be seen in the medallions from Figure 23 at the two rotational speeds with the specification that the pulsation frequency increases with the speed as follows: for $N_{2reduced}$ = 4630 rpm it corresponds a frequency of 1.66 Hz, respectively for $N_{2reduced}$ = 6648 rpm the frequency is 3.63 Hz.

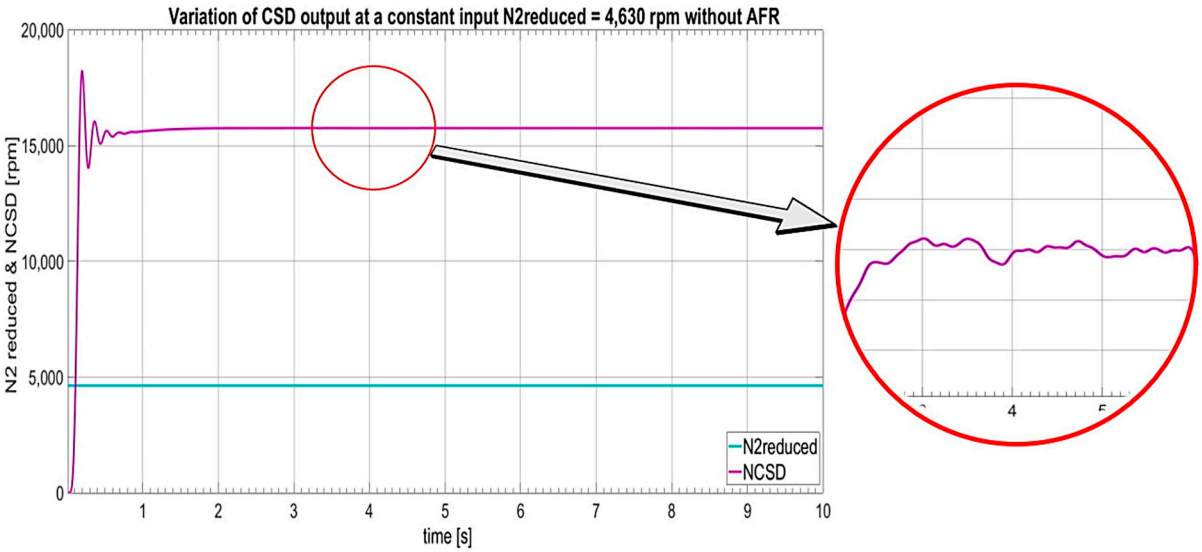

Figure 23. *Cont.*

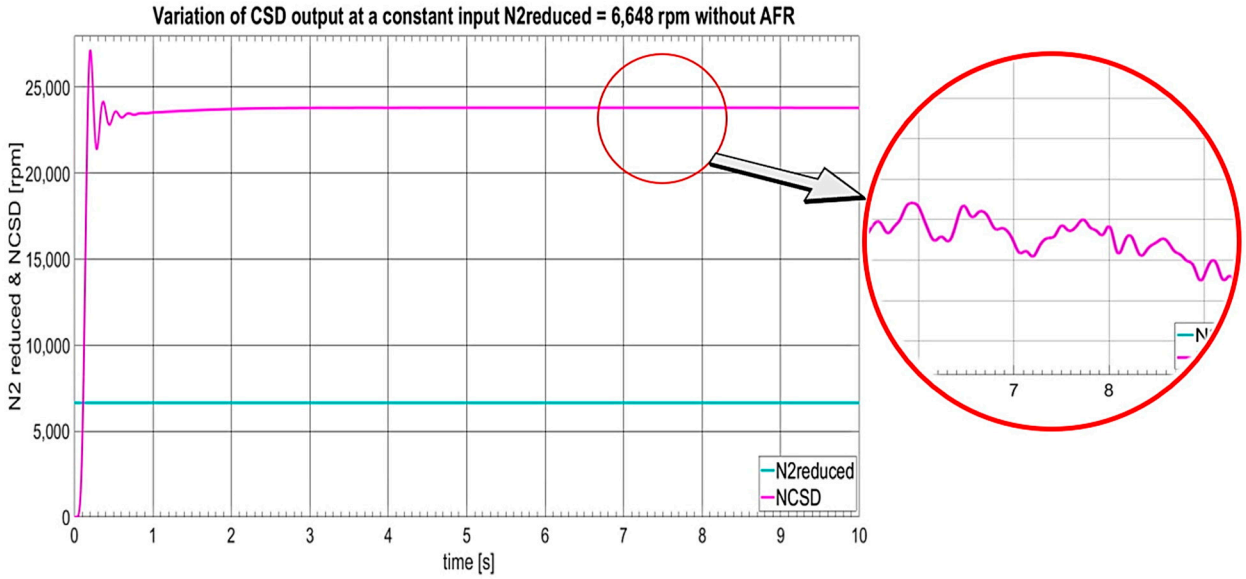

Figure 23. Shape of the output characteristics of the CSD.

Brushless Synchronous Generator Simulink Model

The Simulink model of the BSG shown in Figure 24 is composed of both blocks from the Simulink library and from the Simscape/Power System library and implies their conversion when the signal passes from one mode to another (the SPS and PSS blocks, respectively). The main element is the SG, which has as its input the CSD's rotational speed, converted to angular velocity, and also the two ports for the excitation field. These are obtained from the "SG Field Circuit" block controlled by the V_f obtained from the controller that controls the SG "AC1A Excitation System", an integral part of the AVR in the GCU. As this is in p.u., it is amplified by 20.4 (i.e., $V_{f,\text{base}}$), the maximum value of the SG excitation from Equation (58). The outputs of the SG are the voltages from the *dq0* transformation, V_d and V_q, that are sent as inputs to the AVR in the GCU, and the angular speed of the SG rotor, respectively, which is used by the AFR in the GCU to regulate the rotational speed of the CSD. To connect the SG with the "Secondary electrical distribution" model, both the direct connection using the Power System library and through some interfaces and sensors for the Simulink library are used. Also, to obtain information for the IDG1 panel, from the "Control Panel", the V_abc and I_abc signals, the three-phase peak to peak (p-p) signals, are transformed into rms values and filtered to display relatively constant signals.

The main parameters of B737-800 3-phase, 400 Hz, 2 pole SG rated at 90 kVA driven by CSD at 24,000 rpm are represented in Figure 25 [73,74].

Other important characteristics required for simulation are those specific to the excitation of the synchronous generator. From the manufacturer's documentation, the excitation resistance has a value of 8.5 ohms, and the maximum excitation current is estimated at 2.4 amperes. Thus:

$$R_f = 8.5\Omega; \text{I}_f = 2.4A \Rightarrow \text{V}_f = \text{I}_f \times R_f = 20.4\text{V}, \tag{58}$$

which in p.u. gives:

$$\text{r}_{f,\text{base}} = \frac{\text{V}_\text{f}^2}{R_\text{f}} = 48.96\Omega \Rightarrow \text{r}_f = \frac{R_\text{f}}{\text{r}_{\text{f,base}}} = 0.1736. \tag{59}$$

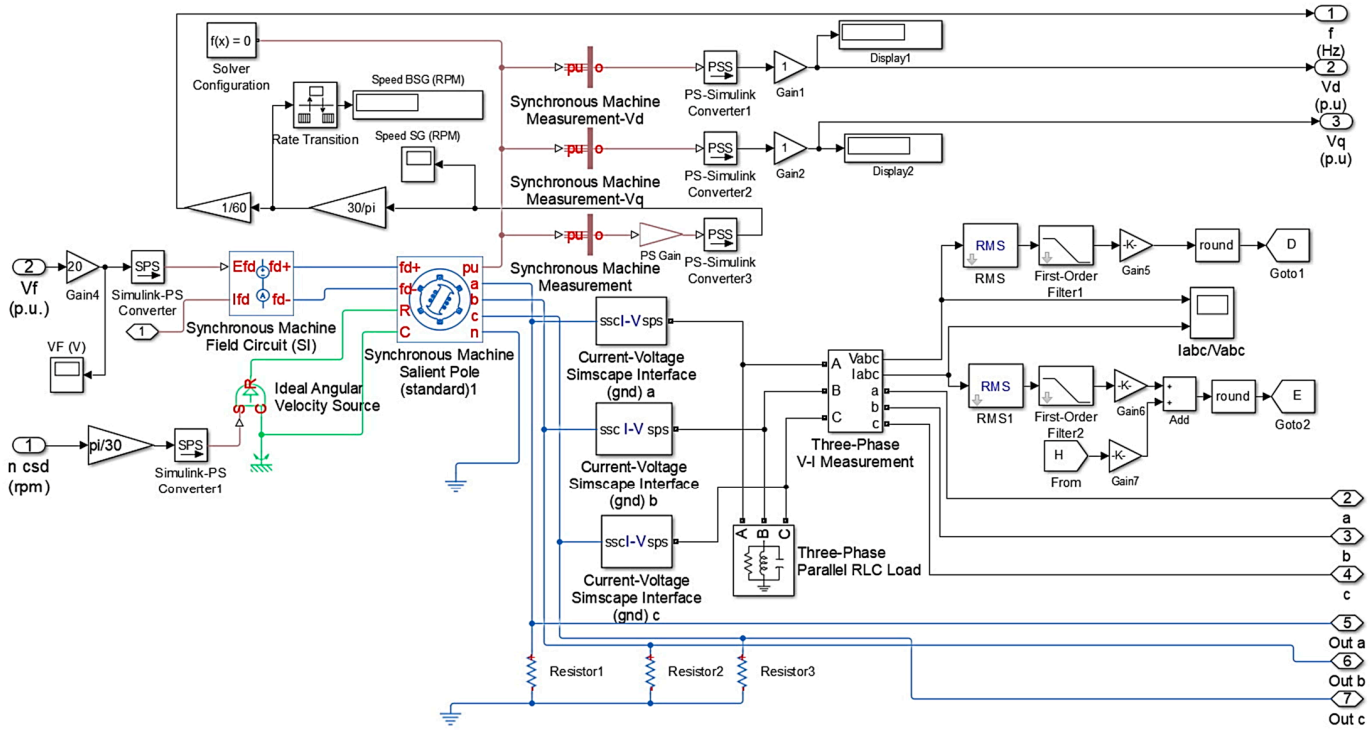

Figure 24. Simulink model for BSG.

4.1.4. Generator Control Unit Simulink Model

As explained in Section 3.3 and represented in Figure 12, the role of this model is to control the frequency of the BSG with the help of the AFR through the CSD and the voltage through the AVR, respectively. The Simulink model of GCU is shown in Figure 26, where the two components, the AFR in green and the AVR in red, were marked.

As the main generator of the BSG is of the synchronous type, in order to be able to supply energy to the airplane's bus, the rotational speed with which it is driven must first be adjusted so that it is equal to the rotational speed corresponding to the operating frequency, stated as 400 Hz. Thus, the adjustment of its rotational speed is achieved with a proportional integral derivative controller (PID) from the discrete library of the Simulink. The PID was tuned according to the Ziegler Nichols tuning rule and also so that the order of magnitude of the tuned output y is within tenths of a millimeter [69], obtaining the values from Figure 27. With these values, the output characteristic of the CSD shown in Figure 28 was obtained, resulting in the best frequency representation, as shown in Figure 29.

If AFR is enabled, it can be seen that the CSD's output rotational speed, of 24,000 rpm, and the corresponding BSG frequency, of 400 Hz, reach steady state in about 2.5 s, well before the entry of the CSD it stabilizes, i.e., after 10 s, and the shape is still pulsating and slightly decreasing.

The AVR was achieved with the IEEE Std 421.5/2016 AC1A excitation system. In order to fit the qualitative parameters of the BSG's voltage in [45,46], the parameters of the AC1A controller were tuned as follows: first, the open circuit voltage is adjusted with K_A to obtain the maximum allowed value. When running under the maximum admissible load, check that V_f reaches the maximum value. Overshoot and settle time adjustment is carried out with T_F. In Figure 30, the results of the simulation, always with the AFR enabled, are represented.

During the first 9 s when the generator is running in open circuit, the voltage stabilizes after approximately 6 s, and when the load is switched on successively, the TRU first, at the 9th second, followed by the first three-phase 25 kW load, at the 17th second and then the second one with the same specifications at the 26th second, the voltage stabilizes approximately in two seconds without exceeding the imposed limits. Also, reaching the

steady state at the mentioned times can be easily seen in Figure 31, and in the time variation of the exciter output voltage.

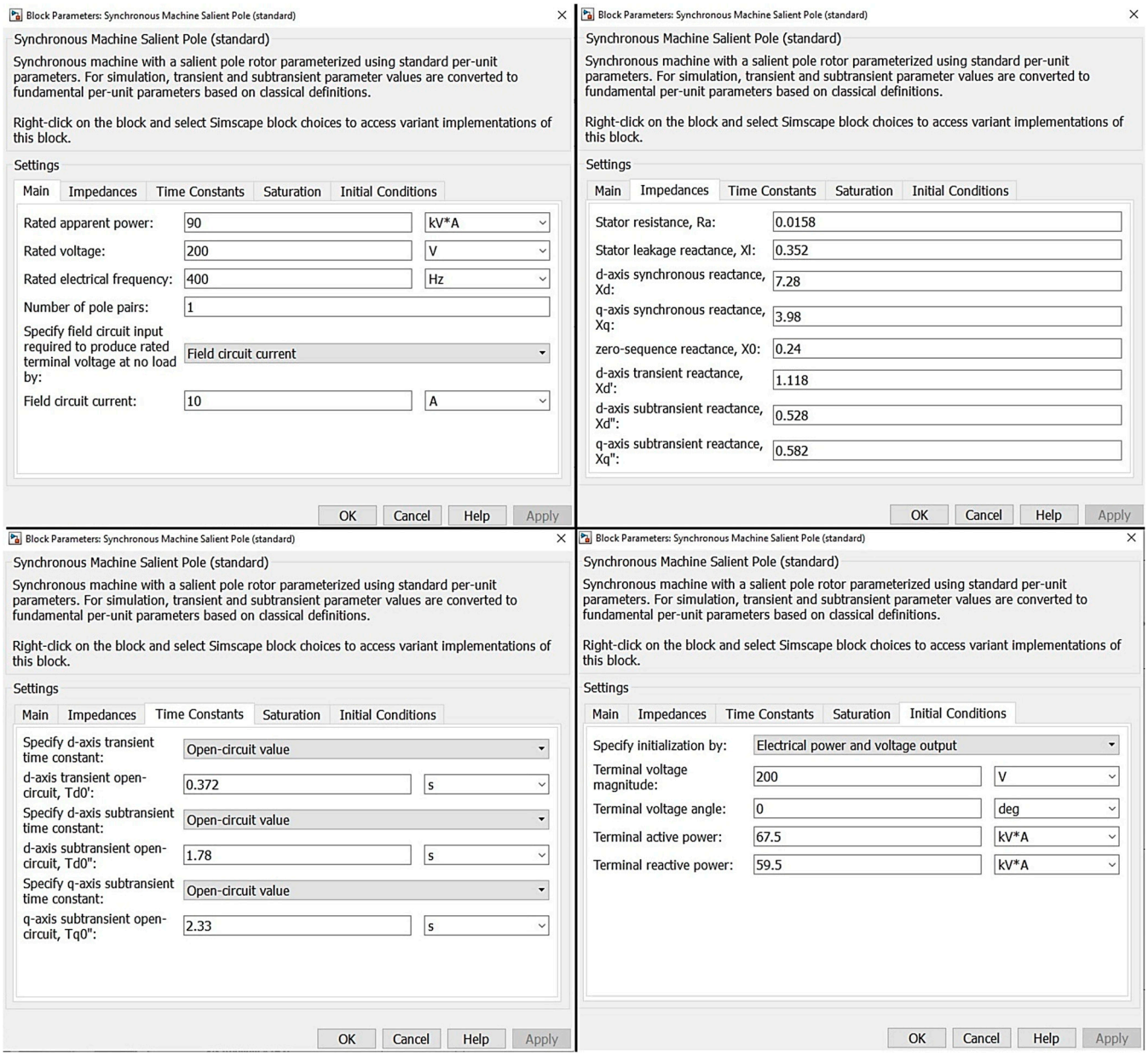

Figure 25. Main characteristics of synchronous generator.

4.1.5. Control Panel Model

This is the device that controls and measures the Simulink model of the EPS. From a structural point of view, it consists of three panels:

1. "Engine 1" used to control and monitor the parameters of the 1st engine and the related CSD;
2. "IDG 1" for monitoring the electrical parameters of the EPS's first channel from the Boeing B737-800 airplane;
3. "Electrical loads", for the control and monitor electrical loads that connect to the plane's electrical busbar.

An attempt to reproduce the architecture of the monitoring panels of the aircraft engine, the CSD and the electrical parameters, as it is on the instrument panel of the

real aircraft, was made. Thus, on the first panel ("Engine 1") from the right from top to bottom, there are three instrument gauges, for the fan rotational speed, N_1 (measured in %), the exhaust gas temperature, EGT (measured in °C), and the core rotational speed, N_2 (measured in %), respectively, all monitored in real time. On the second panel ("IDG 1") from the left to right and top to bottom, the electrical parameters of the DC electrical system, the current ("DC AMPS") and the voltage ("DC VOLTS/") monitored in real time and of the AC electrical system, the frequency ("CPS FREQ"), the current ("/AC AMPS/") and the voltage ("/AC VOLTS"), respectively.

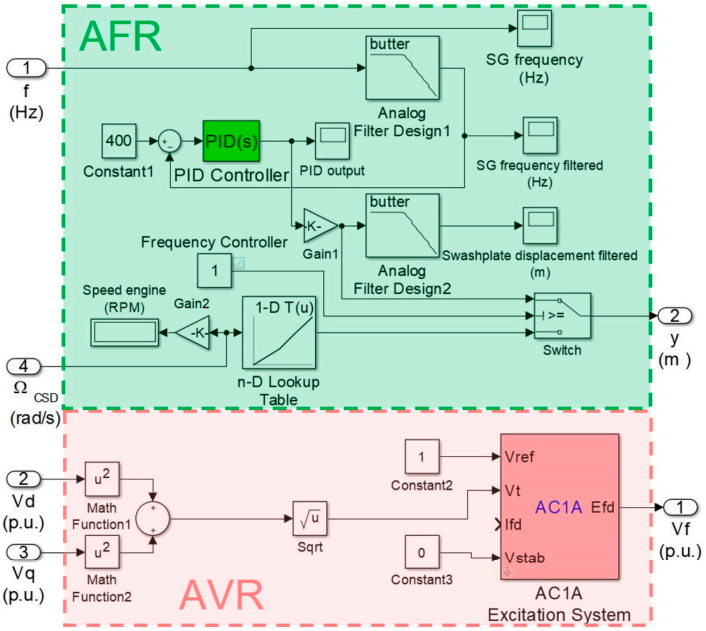

Figure 26. Simulink model for GCU [2].

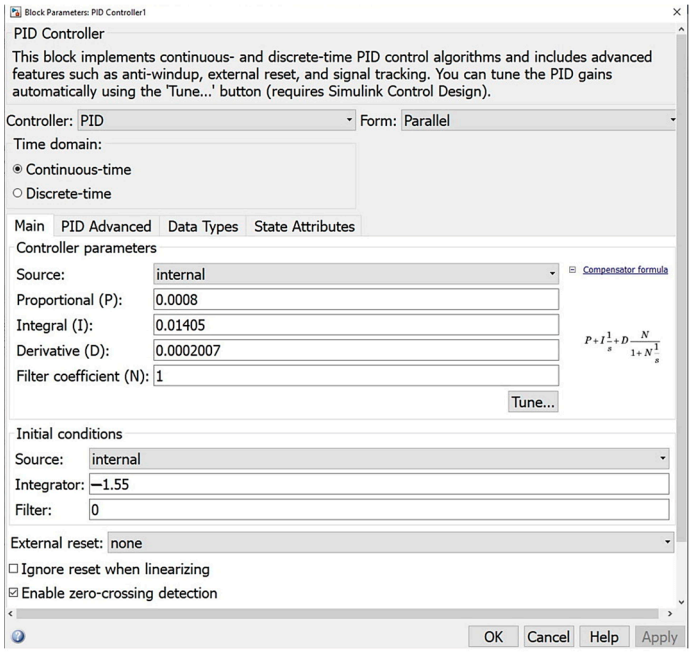

Figure 27. PID parameters.

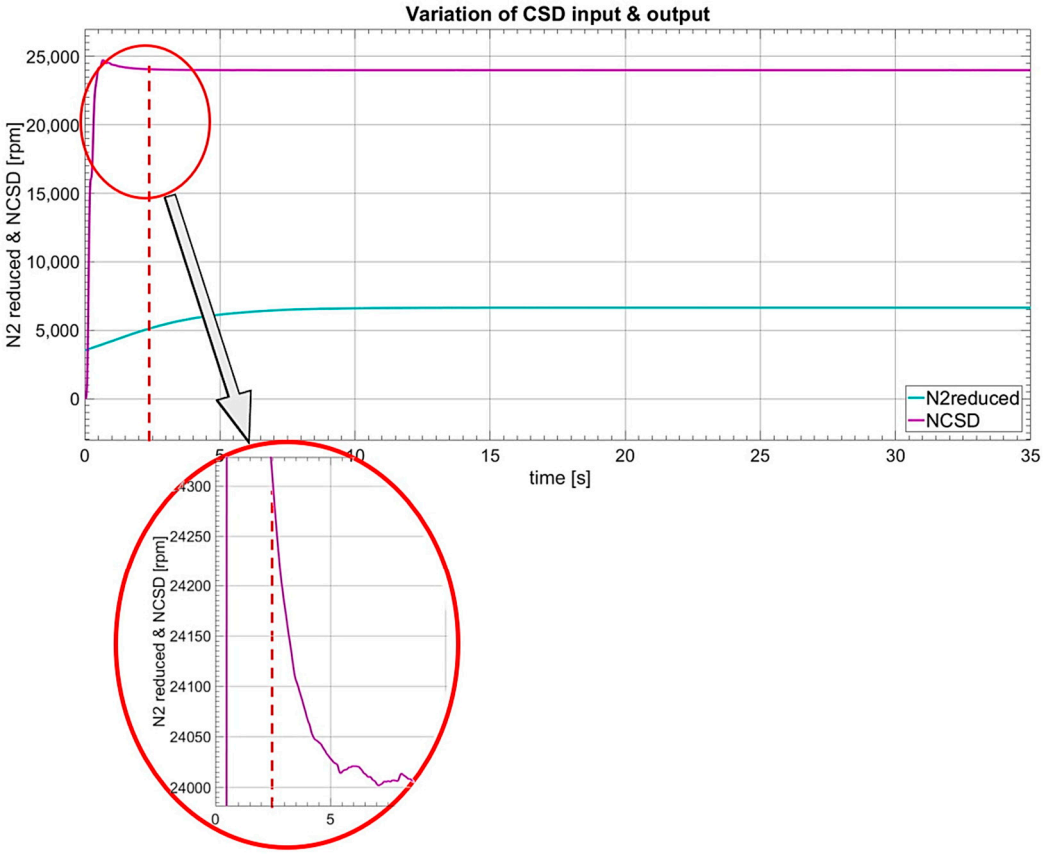

Figure 28. Variation of the CSD characteristics with AFR.

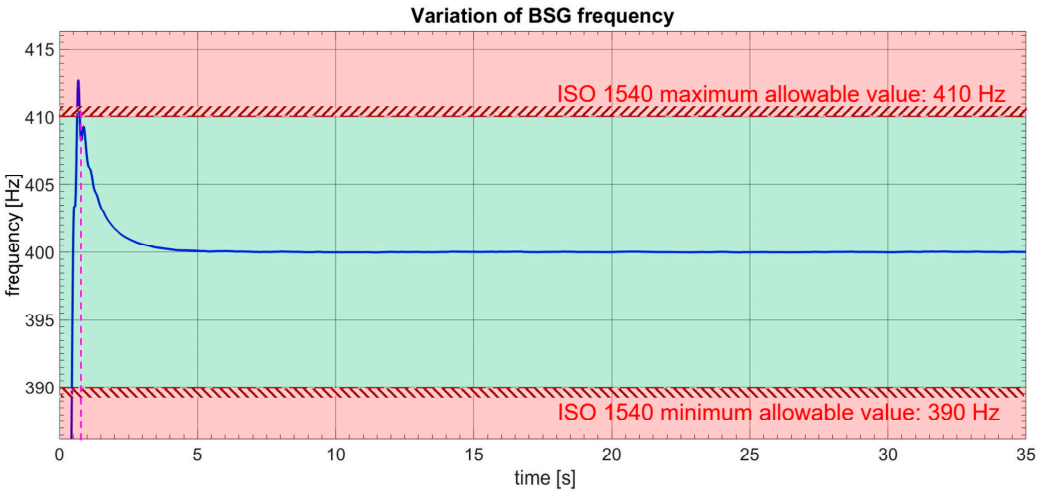

Figure 29. Variation of the BSG frequency compared to the limits in the standard (data limits from [45]).

With the help of the third panel, the three loads can be controlled using three switches, one of direct current through the TRU and two of alternating current. Monitoring of their status, connected or disconnected, was performed using on–off status LEDs.

Thus, referring to the control panel in Figure 14, the state of the system at a steady state in the simulation interval of 35 s is:

- Frequency controller is ON;
- Thrust lever = 0.44;
- N_1 = 57.79% that means $N_1 = 57.79 \times N_{1,100\%}$ = 2990 rpm;

- EGT = 988 °C;
- N_2 = 70.60% that means $N_2 = 70.60 \times N_{2,100\%}$ = 10,209 rpm (value also seen on the left gauge instrument first panel left side);
- DC system: I = 90 A;

  V = 28 VDC;
- AC system: FREQ = 400 Hz (CPS);

  I = 130 A;
  V = 115 VAC;
- TRU DC load is ON;
- 3-phase AC load1 is ON;
- 3-phase AC load2 is ON.

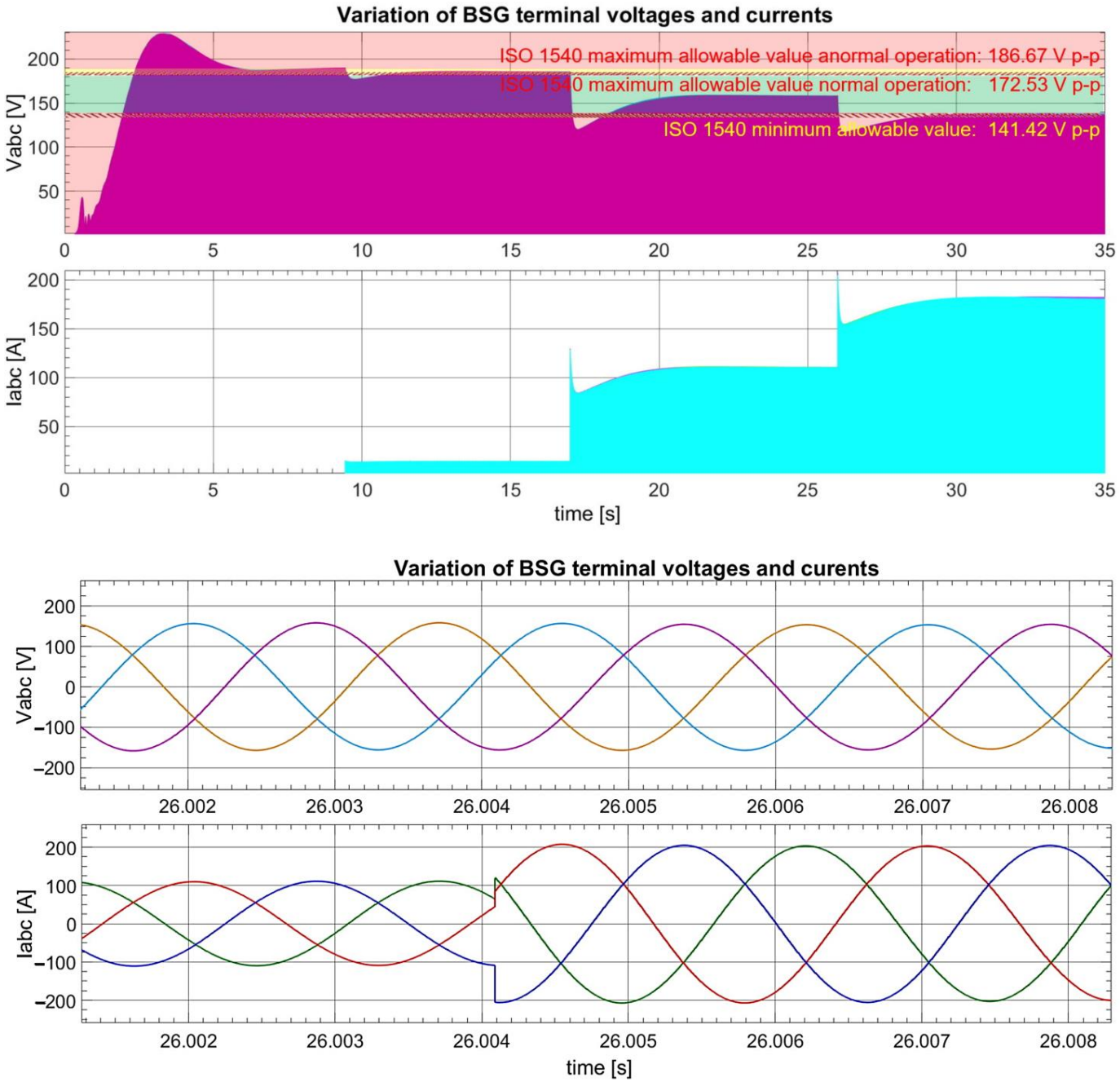

Figure 30. Variation of the BSG terminal parameters compared to the limits in the standard [45].

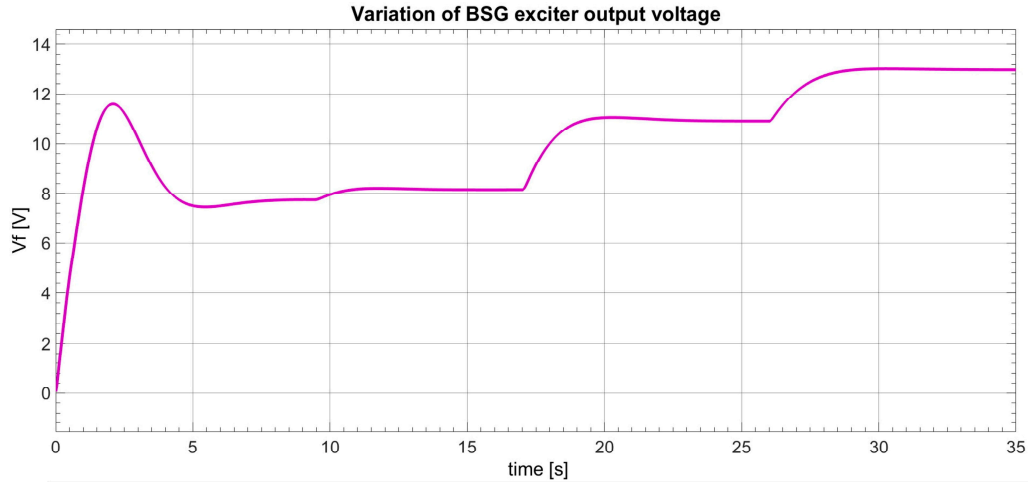

Figure 31. Variation of the BSG exciter output voltage.

Next, the other two scenarios will be analyzed in the same way, and for a better comparison and analysis of the results, they will be presented side by side.

4.2. Simulation of Ground Operation and Loading Scenario

In this phase, the engines start successively; thus, the generators will too. In this step, a small portion of the consumers are loaded, the EPS's protection and loading system, the air-conditioning, the internal, the external and the navigation lights, respectively, and then the initiation and testing of all the aircraft's systems are started. According to the information provided by the operators of this kind of aircraft, in this step, the loading is between 17 and 19%. The general conditions for operating are as follows:

- Altitude: 96 m (considering that the aircraft will take off from Henri Coanda International Airport that is located at this altitude);
- Mach number: 0 (the airplane is at apron for loading);
- Command of the turbofan engine by means of the thrust lever: 0.0269, corresponding to 58% from N_2 on the ground
- Real operation time of aircraft in this scenario: 30 min, that means 14.5% from En route phase [47].

The results of this scenario are represented in Figures 32a, 33a, 34a, 35 and 36a.

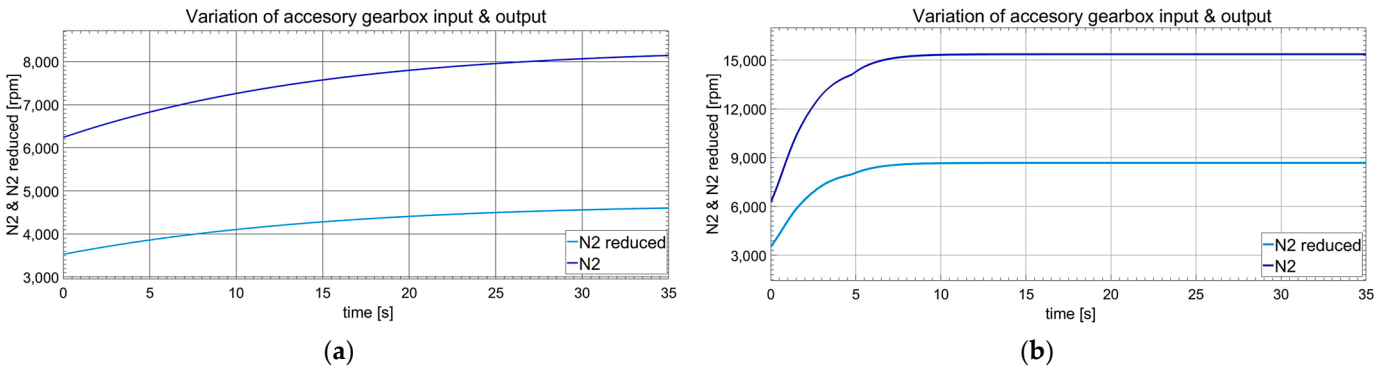

(**a**) (**b**)

Figure 32. Variation of the accessory gearbox characteristics: (**a**) for GOL scenario; (**b**) for ICL scenario.

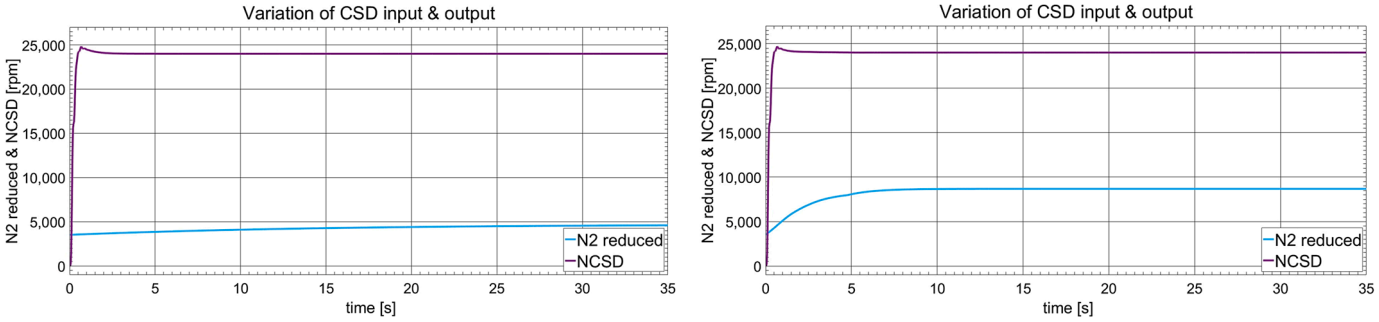

(**a**) (**b**)

Figure 33. Variation of the CSD characteristics: (**a**) for GOL scenario; (**b**) for ICL scenario.

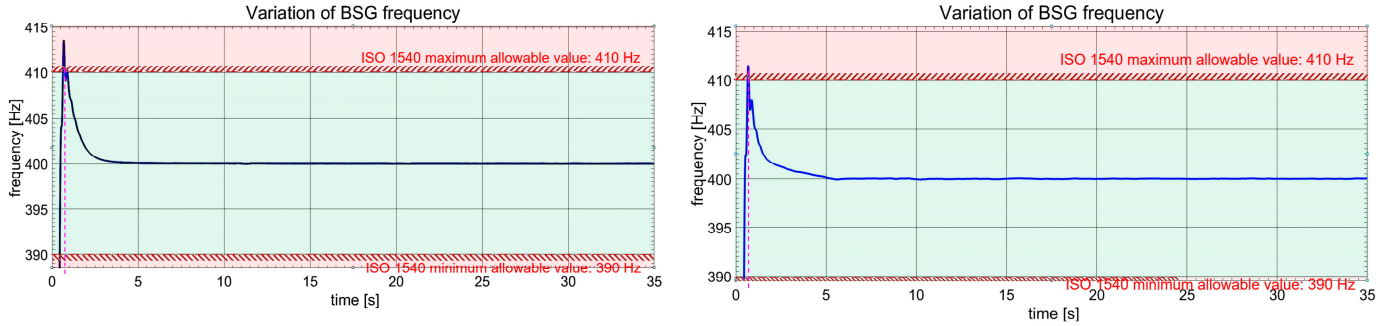

(**a**) (**b**)

Figure 34. Variation of the BSG frequency compared to the limits in the standard (data limits from [45]): (**a**) for GOL scenario; (**b**) for ICL scenario.

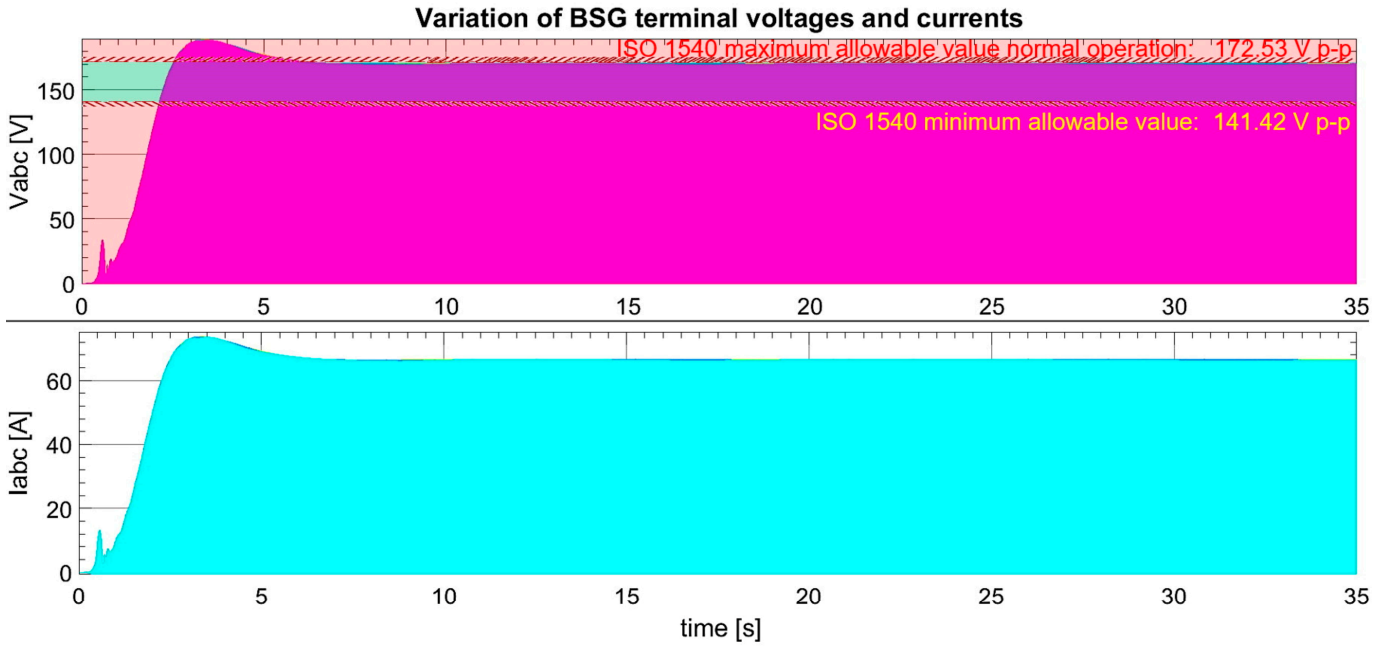

Figure 35. Variation of the BSG characteristics compared to the limits in the standard (data limits from [45]) for GOL scenario.

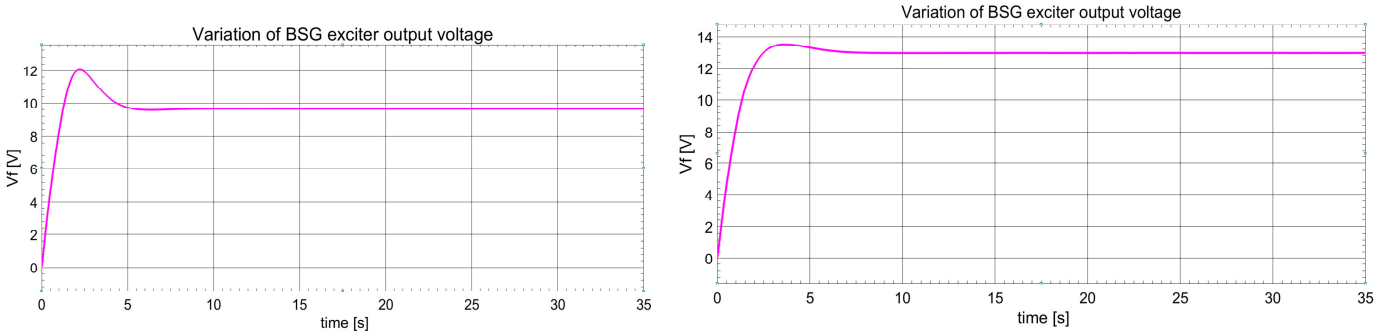

(**a**) (**b**)

Figure 36. Variation of the BSG exciter output voltage: (**a**) for GOL scenario; (**b**) for ICL scenario.

4.3. Simulation of Initial Climb Scenario

ICL is the phase that leads the aircraft into flight cruising, in which all aircraft's systems including the electric one are used at the maximum load, that is, around 60–70%. The general conditions for operating are as follows [75]:

- Altitude: 7315 m;
- Mach number: 0.435;
- Command of the turbofan engine by means of the thrust lever: 0.8, corresponding to maximum thrust, i.e., 105% from N_2 at this altitude;
- Real operation time of aircraft in this scenario: 26 min, that means 12.5% from En-route phase [47].

The results of this scenario are represented in Figures 32b, 33b, 34b, 36b and 37.

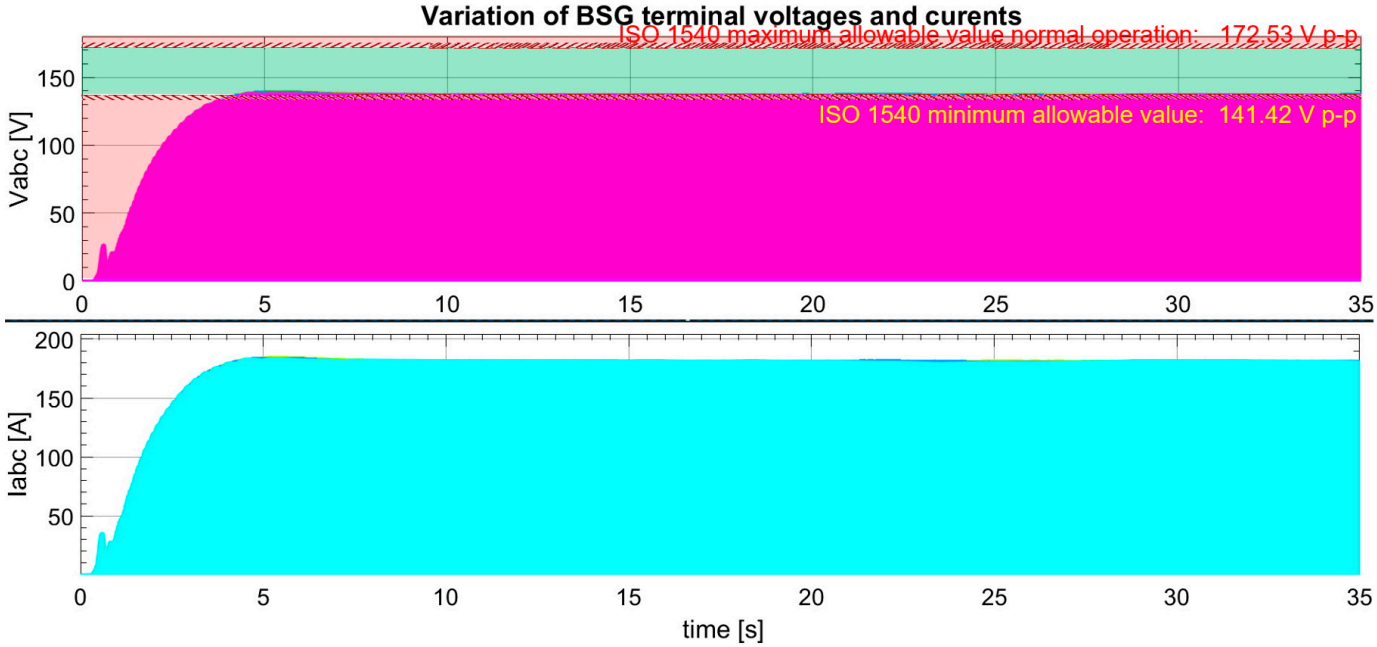

Figure 37. Variation of the BSG characteristics compared to the limits in the standard (data limits from [45]) for ICL scenario.

From Figure 32a, it can be seen that for the GOL phase, the corresponding 58% from N_2 at 96 m is about 8386 rpm, and from Figure 32b for ICL 105% from N_2 at 7315 m is 15,183 rpm, respectively.

From Figure 33a,b, it is very clear that the output characteristic of the CSD in the two scenarios is identical, meaning that the AFR frequency controller works very well, regardless of the N2 speed variation of the turbofan engine.

The CSD drives the synchronous generator with the same characteristic in Figure 34a,b where its frequency is represented and which is also identical.

Once again, as in the first scenario (i.e., En route), from Figure 35 correlated with Figure 36a, and from Figure 36b correlated with Figure 37, it can be seen that the generator's voltages and currents stabilize under 5 s.

5. Discussion

From Figures 29, 30, 34, 35 and 37, it can be seen that the quality parameters of the electricity supplied by BSG fall within the limits of the ISO 1540/2006 standard, including the one related to the waveform of the current and the voltage, which are undistorted, i.e., pure sinusoid. As can be seen from Figure 30, there are only two situations for which there is an exceeding of the voltage value prescribed by the ISO 1540/2006 standard for normal operation (100–122 Vrms equivalent to 141.42–172.53 Vp-p), these two resulting from the operation of the generator in open circuit in the range of 0–9 s when a voltage of 190 V p-p (134 Vrms) is reached, and the operation in the 9–17 s range with the load given by the TRU, when the load is approximately 7 A and a voltage of 186 V p-p (130 V rms) is reached, respectively.

From the discussions with the technical staff of this this aircraft's operators, at no time during the operation of the generator is this run in open circuit, because being a self-excited synchronous generator, it means that it must, at least, cover the consumption with the excitation, which is a maximum of 2.5 A in direct current, the equivalent of 0.514 A in alternating current. In addition to this, at least the GCU (0.5 A), the electrical system and the generator protection devices (approx. 1.5 A), the fuel and hydraulic pump relays (4–5 A) related to engine one and the signal lights (2 A) are always powered, which leads to a total of minimum consumption of approximately 10 A, the current at which the voltage at the generator terminals confirmed by the graph is below the value prescribed by the standard, 122 V rms. Thus, the value indicated by them, as underlined above, is around 17–19%, depending on the aircraft's configuration. The En route step in the EPS simulation is also rather more theoretical, as it is less probable to have an aircraft in flight with the generators running at idle. Despite this, the scenario was introduced to show the behavior of the system to extreme loading variations

Also, the slightly larger variation in the voltage with the generator load can also be attributed to the fact that not all the original electrical parameters of the 90 kVA three-phase generator fitted to the Boeing B737-800 aircraft were found, some of them being extrapolated from aviation generators with different powers and drive speeds from the specialized literature [71,72].

6. Conclusions

This paper presents, for the first time in the specialized literature, a complete simulation of an aircraft's electrical power system using Simulink/Matlab software. For the first time, the BSG is driven by a model of an aircraft turbofan engine via a CSD, as, normally, it happens in reality. By comparing the representations from the three scenarios, it can be seen that both the frequency and the voltages are regulated within the standard limits without any influence from the flight conditions (altitude, speed). Moreover, segments from the representations with similar entry data are identical (as seen in Figure 30 from En route scenario and in Figure 37 from Climb in scenario, respectively, for which the generator loading is the same, 56kW, for the first scenario from second 26, and for the second, with constant load for all the duration of the simulation), meaning that the model developed is robust. One of the challenges was adjusting the AC1A voltage regulator to achieve the power quality parameters, as regulated by the standards, for the reasons explained in the section above.

As a utility of this simulation, working together with the "Microsoft flight simulator", with which Matlab can communicate [76], it is possible to calculate, in real time, the electricity consumption in different stages of the flight for various scenarios, which can lead to an optimization, not only of consumers but also of energy sources.

Funding: This research received no external funding.

Data Availability Statement: The original contributions presented in the study are included in the article; further inquiries can be directed to the corresponding author.

Conflicts of Interest: The author declares no conflicts of interest.

Abbreviations

ACARE	Advisory Council for Aeronautics Research in Europe;
AFR	Automatic frequency regulator;
AE	Aircraft Engine;
AGD	Axial Gear Differential;
AVR	Automatic voltage regulator;
BADA	Base of Aircraft Data;
BBC	Brown-Boveri Company;
Corsia	Carbon Offsetting and Reduction Scheme for International Aviation;
cv	control volume;
ICAO	International Civil Aviation Organization;
IDGS	Integrated Drive Generator System;
ISA	International Standard Atmosphere;
SI	International System of Units;
TE	Turbofan Engine.

References

1. Grigore-Müler, O. Modeling of an Aircraft Constant Speed Drive. *Rev. Roum. Des Sci. Technol. –SÉRIE Électrotechnique Et Énergétique* **2022**, *67*, 487–492.
2. Grigore-Müler, O. Modeling and Simulation of an Aircraft Electrical Power System. *Rev. Roum. Des Sci. Tech. –SÉRIE Électrotechnique Et Énergétique* **2023**, *68*, 224–231. [CrossRef]
3. Researching the Wright Way. Available online: https://airandspace.si.edu/explore/stories/researching-wright-way#propulsion (accessed on 12 July 2024).
4. Brock, W.L. Light Engines. *Am. Mag. Aeronaut.* **1907**, *5*, 29–30.
5. Iatrou, K. *100 Years of Commercial Aviation*; Hermes Air Transport Club: Montreal, QC, Canada, 2014; pp. 20–21.
6. Armstrong, E.R. The construction of the modern aeroplane. *Aero* **1912**, *4*, 239–240.
7. Percy, N. The New York Show attracts public interest. *Aero* **1912**, *4*, 169–170.
8. Bertinov, A.I. *Aviatsionnyye Elektrichskiye Machiny (Aircraft Electrical Generators)*; Oboronnoy Promyshlennosti: Moskva, Russia, 1959; pp. 5–6.
9. Nemkov, V.S. Role of Prof. In V.P. Vologdin and his school in radio and electrotechnology. In Proceedings of the IEEE EUROCON 2009, St. Petersburg, Russia, 18–23 May 2009; pp. 1020–1027. [CrossRef]
10. Sikorsky, I.I. *The Story of the Winged-S*; Dodd, Mead & Company Inc.: New York, NY, USA, 1958; pp. 95–96.
11. Weir, J.G. *The 12 Cylinder Liberty Aero Engine Handbook*; Central House: London, UK, 1918; pp. 61–67.
12. Hyder, A.K. A Century of Aerospace Electrical Power Technology. *J. Propuls. Power* **2003**, *19*, 1155–1179. [CrossRef]
13. Holliday, T.B. Applications of Electric Power in Aircraft. *Electr. Eng.* **1941**, *60*, 218–225. [CrossRef]
14. The integrated drive generator. *Aircr. Eng. Aerosp. Technol.* **1974**, *46*, 9–10. [CrossRef]
15. Airline Business. Available online: https://www.flightglobal.com/airline-business/fleets (accessed on 12 July 2024).
16. Ahmed, F.E. *Aircraft Propulsion and Gas Turbine Engines*, 2nd ed.; Taylor & Francis: Boca Raton, FL, USA, 2017; pp. 4–6+16–18.
17. Meher-Hornji, C.B. The Development of the Whittle Turbojet. In Proceedings of the International Gas Turbine and Aeroengine Congress and Exhibition, Orlando, FL, USA, 2–5 June 1997.
18. Vladimir Pavlecka: Tape #3. Available online: https://vladimirhpavlecka.com/uploads/download/884/Tape__3_-_Conversations_with_Vladimir_Pavlecka.pdf (accessed on 12 July 2024).
19. Trancossi, M.; Pascoa, J. *Thermojet: An Old Idea Can Define a Novel Family of Jets*; SAE Technical Paper 2013-01-2205; SAE International: Warrendale, PA, USA, 2013.
20. History of Flight Around the World. Available online: https://www.aiaa.org/about/History-and-Heritage/History-of-Flight-Around-the-World#romania (accessed on 12 July 2024).
21. Flack, R. *Fundamentals of Jet Propulsion with Applications*; Cambridge University Press: New York, NY, USA, 2005; pp. 6–8+36–38.

22. Early Gas Turbines. Available online: https://www.enginehistory.org/GasTurbines/EarlyGT/XT37/XT37(01).shtml (accessed on 12 July 2024).
23. *Hamilton Sundstrand Brochure*; Hamilton Sundstrand, A United Technologies Company: Windsor Locks, CT, USA, 2008.
24. Nosley, C.C.; Hucker, J.D. Constant Frequency AC Electrical System for Business Aircraft. *SAE Trans.* **1968**, *77*, 728–735.
25. F4H Features Unique Hydraulic Constant Speed Drive System. *Air Force Space Dig.* **1961**, *44*, 55–56.
26. Nordeen, L.D. Roller Friction Transmission. U.S. Patent US3410146, 12 November 1968.
27. Schofield, C.R.; Bradford, E. Variable-ratio Frictional Drive Gears. U.S. Patent US3455177, 20 July 1969.
28. Sharpe, R. Variable Speed Transmission Systems. U.S. Patent US4281559, 4 August 1981.
29. Goi, T. T-IDG Technology Overview. In Proceedings of the Europe-Japan Symposium: Electrical Technologies for the Aviation of the Future, EU Delegation, Tokyo, Japan, 26–27 March 2015.
30. Yoshimura, S. State-of-the-art P1 patrol aircraft to be deployed all over Japan. *The Asahi Shimbun*, 30 July 2019.
31. Paris: C-2, P-1 Underpin Big Japanese Presence. Available online: https://www.flightglobal.com/fixed-wing/paris-c-2-p-1-underpin-big-japanese-presence/133112.article (accessed on 3 September 2024).
32. Burns, J. *Constant Speed Generating Systems*; SAE Technical Paper 771001; SAE International: Warrendale, PA, USA, 1977.
33. Griffiths, J.T.; Sharpe, R. Electric Generator Arrangement. U.S. Patent US4278928, 14 July 1981.
34. Cordner, A.M.; Flygare, A.W.; Grimm, H.D. Integrated Drive-generator System. U.S. Patent US4252035, 24 February 1981.
35. Gantzer, C.J. Combined Fluid and Mechanical Drive. U.S. Patent US3365981A, 30 January 1968.
36. Manring, N.D. The Discharge Flow Ripple of an Axial-Piston Swash-Plate Type Hydrostatic Pump. *J. Dyn. Syst. Meas. Control* **2000**, *122*, 263–268. [CrossRef]
37. Guan, C.; Jiao, Z.; He, S. Theoretical study of flow ripple for an aviation axial-piston pump with damping holes in the valve plate. *Chin. J. Aeronaut.* **2014**, *27*, 169–181. [CrossRef]
38. Aron, I.; Păun, V. *Echipamentul Electric al Aeronavelor*; Ed. Didactică și Pedagogică: București, Romania, 1980; pp. 277–279.
39. Dinu, D. *Mașini Hidraulice și Pneumatice Utilizate în Domeniul Naval*; Ed. Nautica: Constanța, România, 2019; pp. 33–35.
40. The Sperry Gyroscope, Co. *Flight*; The Sperry Gyroscope Co.: Downtown Brooklyn, NY, USA, 1915; Volume 7, pp. 20–21.
41. Hyland, L.A. Airplane Radio Sets. *Aviation* **1927**, *XXIII*, 1526–1528.
42. Airways and Airports, Blind landing System Conquers Fog. In *The Aircraft Year Book for 1935*; Aeronautical Chamber of Commerce of America: New York, NY, USA, 1935; Volume 17, pp. 207–208.
43. Sperry, E.A. Wind-Driven Generator for Aircraft. U.S. Patent US1362753, 21 December 1920.
44. Kundur, P. *Power System Stability and Control*; McGraw-Hill: New York, NY, USA, 1994; pp. 75–88.
45. *ISO1540*; Aerospace–Characteristics of Aircraft Electrical Systems. 3rd ed. ISO: Geneva, Switzerland, 2006.
46. *MIL-STD-704F w/CHANGE 1*; Aircraft Electric Power Characteristics. Department of Defense: Arlington County, VA, USA, 2016.
47. Grigore-Müler, O. *Aircraft Electrical Power System: Analysis and Design*; Ed. MATRIX ROM: București, Romania, 2021; pp. 177–179+495–496.
48. *IEEE Std 421.5*; IEEE Recommended Practice for Excitation System Models for Power System Stability Studies. IEEE: Piscataway, NJ, USA, 2016.
49. Else, H.D.; Basel, D.R.; Braun, H.J.; Township, S. Liquid-Cooled Dynamoelectric Machine. U.S. Patent US2862119 Patent, 25 November 1958.
50. Boeing Delivered Final Commercial 737NG in January, Ending 23 Years of Production. Available online: https://www.flightglobal.com/airframers/boeing-delivered-final-commercial-737ng-in-january-ending-23-years-of-production/137879.article (accessed on 1 August 2024).
51. How Many Boeing 737 Aircraft Are Currently in Service & Stored? Available online: https://simpleflying.com/boeing-737-in-service-stored/ (accessed on 1 August 2024).
52. Efimov, A.A.; Melinkov, S.Y.; Garganeev, A.G. Simulation of aircraft electrical power supply system. In Proceedings of the IV International Conference on Information Technologies in Engineering Education, Moscow, Russia, 23–26 October 2018.
53. Tantawy, A.; Koutsoukos, X.; Biswas, G. Aircraft generators: Hybrid Modeling and simulation for fault detection. *IEEE Trans. Aerosp. Electron. Syst.* **2012**, *48*, 552–571. [CrossRef]
54. Bruck, F.M.; Himmelstoss, F.A. Modelling and simulation of a synchronous machine. In Proceedings of the COM.P.EL.98. Record 6th Workshop on Computer in Power Electronics (Cat. No.98TH8358), Cernobbio, Italy, 22 July 1998.
55. Michna, M.; Kutt, F.; Chrzan, P.; Ronkowski, M. Modeling and analysis of a synchronous generator in more electric aircraft power system using synopsys/Saber simulator. *Pr. Elektrotechniki* **2009**, *240*, 31–46.
56. Li, X.; Kher, S.; Huang, S.; Ambalavanar, V.; Hu, Y. Component modeling and system level simulation of aircraft electrical systems. *Eng. Lett.* **2016**, *24*, 178–186.
57. Kurtoglu, T.; Bunus, P.; De Kleer, J.; Rai, R. Simulation-based design of aircraft electrical power systems. *Linköping Electron. Conf. Proc.* **2011**, *63*, 704–712.
58. Dinesh, G.; Viswa, A.B.; Vedula, V. Modeling of a traditional aircraft generator and its subsystems. In Proceedings of the 2015 IEEE International Conference on Electrical, Computer and Communication Technologies, Coimbatore, India, 5–7 March 2015.
59. Ruiz, L.; Inca, G.; Bautista, R.; Arevalo, E. Simulation of a Boeing 737-500 Aircraft Electrical System. In Proceedings of the 2022 IEEE Sixth Ecuador Technical Chapters Meeting, Quito, Ecuador, 11–14 October 2022.

60. CCITT Phase of Flight–Definitions and Usage Notes, v 1.3, April 2013. Available online: https://www.intlaviationstandards.org/Documents/PhaseofFlightDefinitions.pdf (accessed on 4 October 2024).
61. *Aeronautical Vestpocket Handbook*, 22nd ed.; United Technologies Pratt & Whitney, Commercial Engine Business Government Engines and Space Propulsion Operations: West Palm Beach, FL, USA, 1991; pp. 137–138.
62. Howe, D. *Aircraft Conceptual Design Synthesis*; Professional Engineering Publishing Limited: London, UK; Bury St Edmunds, UK, 2000; pp. 65–67.
63. Turbofan Engine System. Available online: https://www.mathworks.com/help/aeroblks/turbofanenginesystem.html (accessed on 11 August 2024).
64. Nuic, A.; Poles, D.; Mouillet, V. BADA: An advanced aircraft performance model for present and future ATM systems. *Int. J. Adapt. Control Signal Process.* **2010**, *24*, 850–866. [CrossRef]
65. Flight Ops/Engines. Available online: https://www.smartcockpit.com/download/cfm-flight-ops-support-b737/?wpdmdl=3229&refresh=66d705b33ae941725367731 (accessed on 3 September 2024).
66. TCDS, No.: E.004 Issue: 05 for CFM International CFM56-7B Series Engine, EASA, 1 March 2016. Available online: https://www.easa.europa.eu/en/document-library/type-certificates/engine-cs-e/easae004-cfm-international-sa-cfm56-7b-series (accessed on 3 September 2024).
67. Yılmaz, İ. Evaluation of the relationship between exhaust gas temperature and operational parameters in CFM56-7B engines. *Proc. Inst. Mech. Eng. Part G J. Aerosp. Eng.* **2009**, *223*, 433–440. [CrossRef]
68. Hydraulic Axial-Piston Pump with Load-Sensing and Pressure Limiting Control. Available online: https://www.mathworks.com/help/hydro/ug/hydraulic-axial-piston-pump-with-load-sensing-and-pressure-limiting-control.html (accessed on 26 July 2022).
69. Campbell, K.H.; Lemmers, G.C., Jr.; Franklin, M.J. Cylinder Block Assembly for Hydraulic Unit. U.S. Patent US20160273531A1, 22 September 2016.
70. Hochstetler, D.R.; Martin, T.A.; Johnson, D.C.; Lemmers, G.C., Jr. Hydraulic Unit Cylinder Block for Integrated Drive Generator. U.S. Patent US10539213B2, 21 January 2020.
71. Hochstetler, D.R.; Martin, T.A.; Johnson, D.C.; Lemmers, G.C., Jr. Variable Wobbler Plate for Integrated Drive Generator. U.S. Patent US10707792B2, 7 July 2020.
72. Shop Talk: Change in Hydraulic Fluid, Newsletter, Onboard Systems International. Available online: https://www.onboardsystems.com/news/newsletter/154 (accessed on 26 July 2022).
73. Holloway, V.C. Transient characteristics of aircraft A-C generators. *Trans. Am. Inst. Electr. Eng. Part II Appl. Ind.* **1954**, *73*, 187–190. [CrossRef]
74. Sasaki, R.; Masanao, W.; Osamu, S. Weight and Characteristics of Aircraft AC Generators. *Aeronaut. Space Sci. Jpn.* **1979**, *27*, 296–300.
75. Aircraft Performance Database. Available online: https://contentzone.eurocontrol.int/aircraftperformance/details.aspx?ICAO=B738&GroupFilter=4 (accessed on 4 October 2024).
76. Work with the Flight Simulator Interface. Available online: https://www.mathworks.com/help/aeroblks/working-with-the-flight-simulator-interface.html (accessed on 16 September 2024).